

Chapter 10

Finescale Radar Observations of a Dryline during the International H₂O Project (IHOP_2002)

CHRISTOPHER C. WEISS

Department of Geosciences, Texas Tech University, Lubbock, Texas

HOWARD B. BLUESTEIN

School of Meteorology, University of Oklahoma, Norman, Oklahoma

ANDREW L. PAZMANY

ProSensing, Inc., Amherst, Massachusetts

BART GEERTS

College of Engineering, University of Wyoming, Laramie, Wyoming

(Manuscript received 25 February 2004, in final form 9 March 2006)



Weiss



Bluestein



Geerts

ABSTRACT

A case study of a double dryline on 22 May 2002 is presented. Mobile, 3-mm-wavelength Doppler radars from the University of Massachusetts and the University of Wyoming (Wyoming cloud radar) were used to collect very fine resolution vertical-velocity data in the vicinity of each of the moisture gradients associated with the drylines. Very narrow (50–100 m wide) channels of strong upward vertical velocity (up to 8 m s^{-1}) were measured in the convergence zone of the easternmost dryline, larger in magnitude than reported with previous drylines. Distinct areas of descending motion were evident to the east and west of both drylines. Radar data are interpreted in the context of other observational platforms available during the International H₂O Project (IHOP_2002). A variational ground-based mobile radar data processing technique was developed and applied to pseudo-dual-Doppler data collected during a rolling range-height indicator deployment. It was found that there was a secondary (vertical) circulation normal to the easternmost moisture gradient; the circulation comprised an easterly component near-surface flow to the east, a strong upward vertical component in the convergence zone, a westerly return flow above the convective boundary layer, and numerous regions of descending motion, the most prominent approximately 3–5 km to the east of the surface convergence zone.

Corresponding author address: Christopher C. Weiss, Dept. of Geoscience, Texas Tech University, Box 42101, Lubbock, TX 79409.
E-mail: chris.weiss@ttu.edu

1. Introduction

Fred Sanders was interested in the physical processes responsible for the formation of deep convection (Sanders and Blanchard 1993) and the forecasting of deep

convection (Sanders and Garrett 1975; Sanders 1986). Independent of his interest in convection, he pursued his interest in the analysis, nature, and behavior of surface boundaries, along which ascending motion on the mesoscale sometimes initiates convective clouds (e.g., Sanders and Doswell 1995; Bluestein 2008). In addition, the second author remembers well his interest in synthesizing all available sources of data, including radar data, in studying the behavior of convective systems (e.g., Miller and Sanders 1980). The second author recalls finding Fred Sanders pouring over sequences of radar images that covered much of the 16th floor corridor of the Green Building at the Massachusetts Institute of Technology while he studied the case just referenced. It is in the spirit of Fred's enthusiasm for convection and surface boundaries that we present this recent study of the behavior of a dryline and its relation to convection initiation (CI), which is based on a new, mobile observing system and a new analysis technique.

The processes responsible for the initiation of deep moist convection have intrigued researchers and forecasters alike for decades. Even in cases in which the large-scale environment is conducive to the development of severe thunderstorms (i.e., when there is high potential instability and strong vertical wind shear over a broad area), CI occurs only locally. CI tends to occur in regions where there is mesoscale convergence of winds in the boundary layer, and therefore forced ascent. Surface boundaries are examples in which there can be mesoscale ascent (Bluestein 2008); therefore, much of the ambiguity surrounding the convection initiation problem can be diminished through a better understanding of the finescale motions near these boundaries.

The dryline, in the southern plains of the United States, is an example of a boundary that frequently initiates intense thunderstorms, some of which are responsible for the production of large hail, damaging winds, and tornadoes during the spring months. The dryline can be thought of as the intersection between the top of a surface-based layer of virtually cool, moist air originating over the Gulf of Mexico and the sloping terrain east of the Rocky Mountains. The prediction of CI along this boundary is particularly complex owing to the large fluctuations in the position of, movement of, and convergence along, the boundary.

During the spring months of 2002, the International H₂O Project (IHOP) was conducted over the central and southern plains. The mission of IHOP was the improved characterization of the four-dimensional distribution of water vapor and its application to improving the understanding and prediction of convection (Weckwerth et al. 2004). A multitude of surface and airborne observing platforms were employed through the course of the experiment.

In conjunction with these platforms, W-band (3-mm wavelength; 95 GHz) radars from the University of Massachusetts (UMass) (Bluestein and Pazmany 2000) and the University of Wyoming [Wyoming cloud radar

(WCR)] collected data in a number of drylines during IHOP (Weiss et al. 2006). The narrow half-power beamwidth of the radars (0.18° and 0.7° for UMass and WCR, respectively) allowed for very fine spatial resolution, and thereby the potential existed to resolve scales of motion near the dryline that had been previously unresolved. A better knowledge of these finescale motions will ultimately lead to a more accurate understanding of the success or failure of CI in the dryline convergence zone (DCZ).

Another goal of this project was to develop a retrieval technique to synthesize, from time series of range-height indicator (RHI; i.e., vertical cross sections) data, the two-dimensional wind components in the plane normal to the dryline. Radar velocity observations are inherently one-dimensional, measuring the component of motion toward/away from the radar line of sight. However, using certain assumptions and scanning strategies, the two-dimensional wind field can be recovered.

The purpose of this paper is to describe the analysis technique applied to, and the analysis of, Doppler wind data in drylines on 22 May 2002 during IHOP. Section 2 provides an overview of the development and motion of the drylines. A summary of scanning strategies used by the W-band radar system is presented in section 3. Section 4 details the analysis of data collected with a vertically pointed antenna. Section 5 describes the development and testing of a variational radar synthesis technique, which is applied to data from the drylines, in section 6. Finally, a summary is given in section 7.

2. Overview of dryline motion and development

The early evolution of the 22 May 2002 dryline was typical of that seen over the southern plains. The dryline was located¹ over the western Oklahoma and Texas Panhandles at 1500 UTC (Fig. 1a). Because of the increase in sensible heating during the late morning and early afternoon the boundary layer deepened significantly (not shown), thereby permitting the distinctive eastward advancement of the dryline by 1800 UTC (Fig. 1b). Sharp decreases in dewpoint were noted with dryline passage over Kansas [e.g., Elkhart, Kansas (EHA), and Liberal, Kansas (LBL)]. Farther to the south, surface dewpoints fell in a more gradual manner [e.g., Amarillo, Texas (AMA)], which was less indicative of a distinct dryline passage. This region will be shown to be an intermediate zone between two sharp moisture gradients/drylines later in the day.

By late afternoon the dryline ceased its eastward advancement and stalled over the eastern Oklahoma and

¹ The dryline was analyzed at the leading edge of the sharpest surface dewpoint gradient, when reporting surface stations were available. Data from other sources [e.g., University of Wyoming King Air in situ specific humidity measurements; Weather Surveillance Radar-1988 Doppler (WSR-88D) finelines] were used to provide the best estimate of dryline position in areas void of adequate surface measurements.

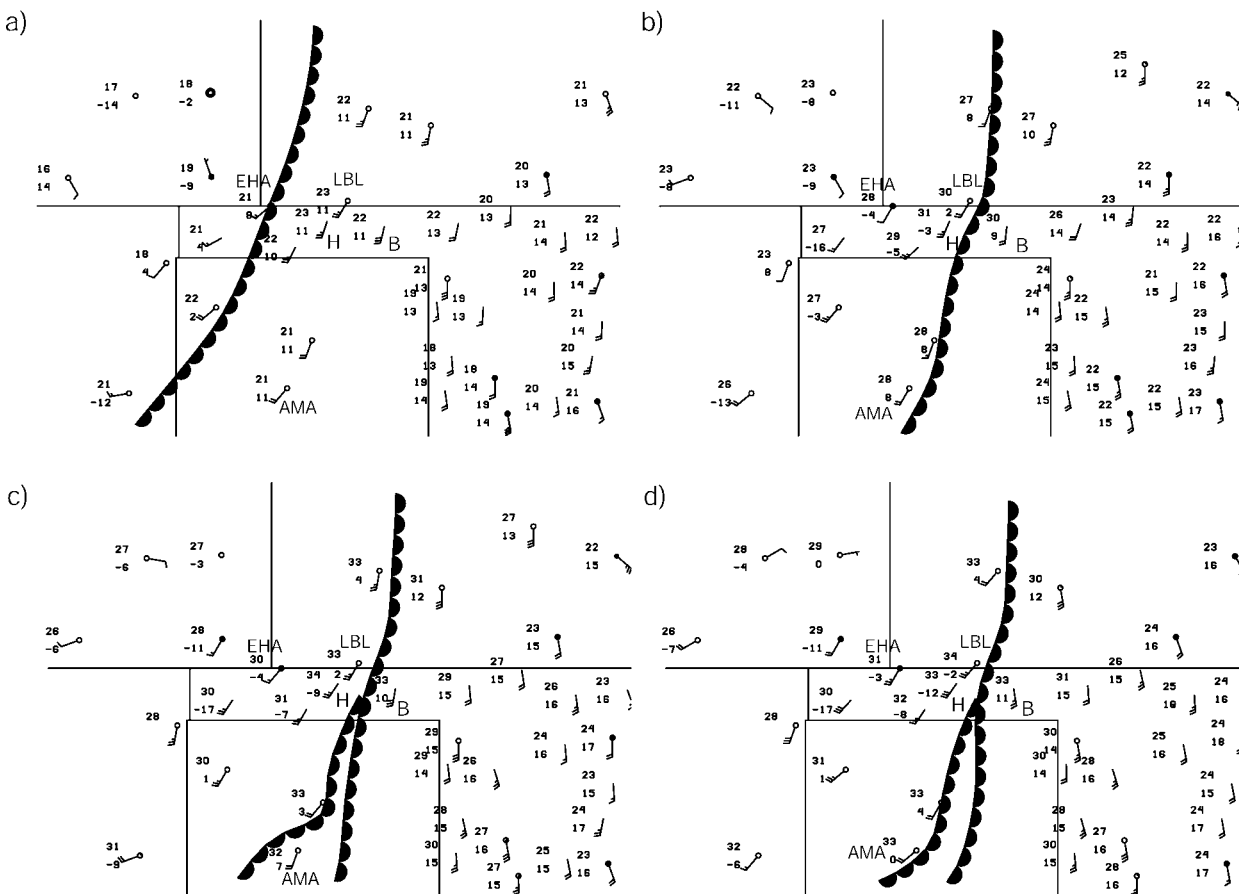


FIG. 1. High plains surface map valid at (a) 1500, (b) 1800, (c) 2100, and (d) 2300 UTC 22 May 2002. Temperature ($^{\circ}\text{C}$) and dewpoint ($^{\circ}\text{C}$) for each station are shown. Full (half) wind barbs denote 5 (2.5) m s^{-1} . The scalloped lines indicate the position of (known) drylines. The labels EHA, LBL, AMA, H, and B denote the locations of Elkhart, KS, Liberal, KS, Amarillo, TX, Hooker, OK, and Beaver, OK, respectively.

Texas Panhandles. The dewpoint gradient sharpened considerably during this time, and by 2100 UTC (Fig. 1c) a dewpoint difference of 18°C was evident over the 60 km between Hooker, Oklahoma, and Beaver, Oklahoma. Convergence was also evident on the boundary at this time. The magnitude of this convergence varied considerably as winds were gusty on both sides of the dryline. As seen earlier, the dewpoint at AMA continued to decrease in a steady manner until 2200 UTC, when there was a sharp decrease from 7° (2200 UTC) to 0°C (2300 UTC; Fig. 1d).

It is seen in WSR-88D radar reflectivity data from Amarillo (KAMA) at about 2300 and 0000 UTC (Figs. 2a,b) that there was a double-fine line (i.e., thin maximum in reflectivity) structure over the northern Texas Panhandle.² The passage of the westernmost fine line

coincided with the sharp dewpoint decrease observed at AMA at 2300 UTC (Figs. 1c,d). Earlier in the afternoon, AMA was situated between the finelines and experienced a gradual decrease in dewpoint. This behavior was in accord with that observed in other studies (e.g., Hane et al. 1997; Crawford and Bluestein 1997). The two finelines were oriented such that they merged just to the north of the 10-cm wavelength, dual-polarization National Center for Atmospheric Research (NCAR) S-band dual polarization (SPOL) radar (<http://www.atd.ucar.edu/rsf/spol/spol.html>) at Homestead, Oklahoma (Fig. 3a). It is apparent in visible satellite imagery (Fig. 4) that there was a wedge-shaped area of cumulus cloud cover in the region between the radar finelines over the Oklahoma and northern Texas Panhandles (Figs. 2a,b and 4). A time series of in situ dewpoint measurements taken at 800 m AGL aboard the University of Wyoming King Air (UWKA) (Geerts and Miao 2005) supported the coexistence of separate moisture gradients with each fine line (Figs. 3a,b). It is noted that the domain of UMass operations (white box in Fig. 3a) on this day was to the south of the intersection point.

² Finelines are often used as evidence of confluence in the dryline convergence zone, as the insect concentration, and therefore radar reflectivity, locally increases in these regions. Because the region of confluence is where the strongest frontogenesis is also occurring, the sharp specific humidity gradient at the dryline is often correlated with a thin reflectivity fine line.

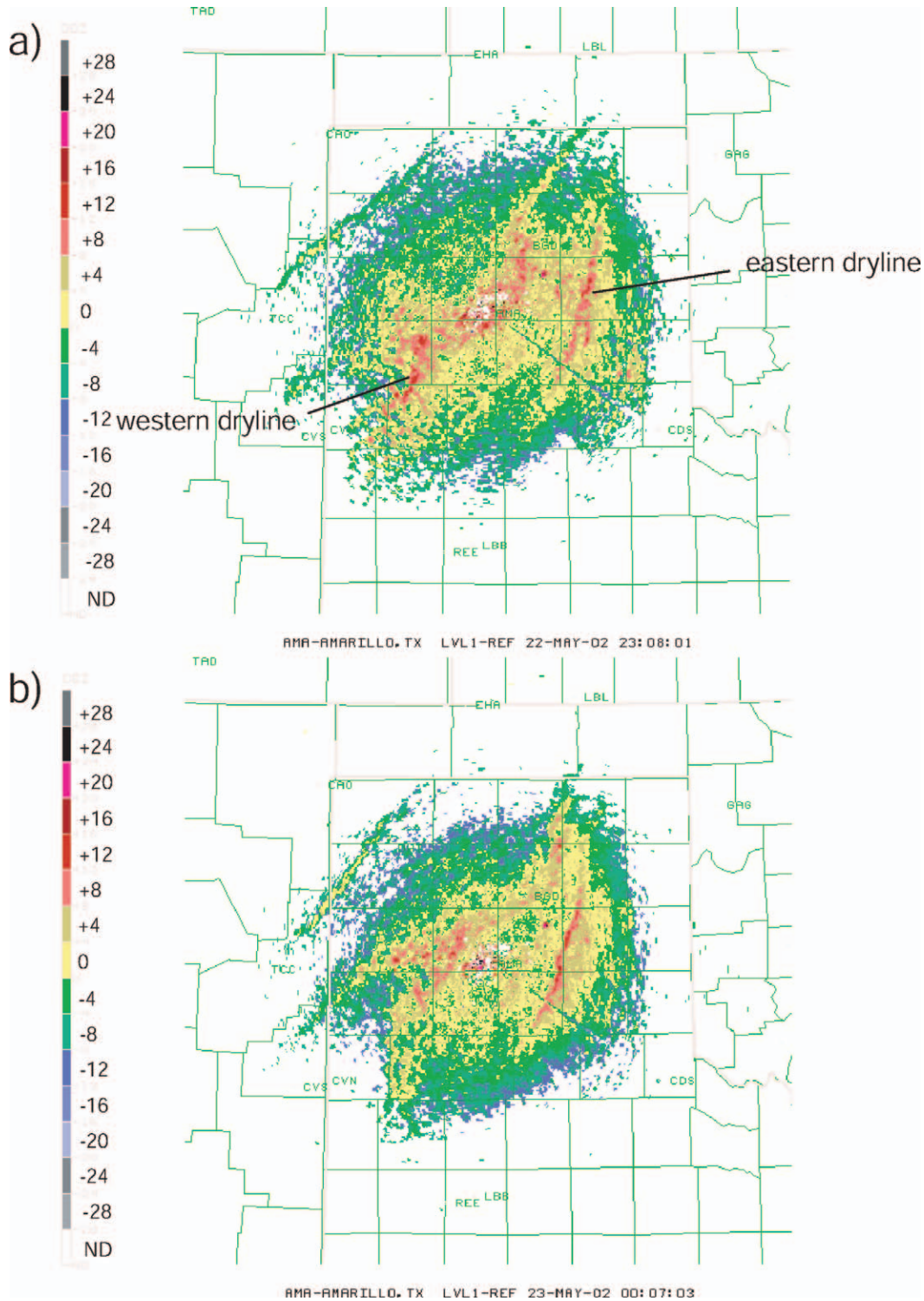


FIG. 2. WSR-88D 0.5° reflectivity (dBZ) at Amarillo valid at (a) 2308 UTC 22 May 2002 and (b) 0007 UTC 23 May 2002. Reflectivity scale provided to the left. The locations of the eastern and western dryline are shown in (a). (c) 0.5° reflectivity (dBZ) from the SMART-R at 2254 UTC 22 May 2002. The black arrow indicates the path of the UMass vertical antenna deployment. Note that these data were collected approximately 20 min after the termination of the UMass vertical antenna deployment. The locations of the eastern and western dryline are shown. Range markers are indicated in black.

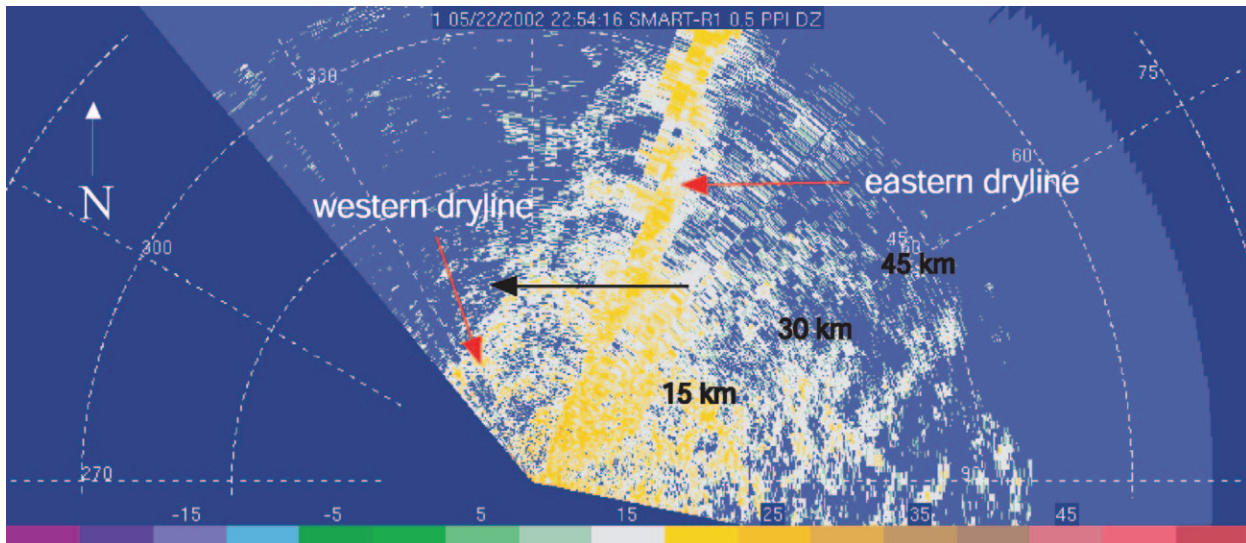


FIG. 2. (Continued)

Therefore, the data collection encompassed both drylines. Both dryline boundaries demonstrated retrogression by 0000 UTC (Figs. 2a,b).

Deep convection had initiated along the dryline over northwestern Kansas and eastern Nebraska by late in the afternoon. This region was more directly influenced by a longwave trough over the western United States (not shown), which likely produced vertical motion and midlevel cooling that aided in the development of the convection. Farther to the south, no sustained deep convection was initiated along the dryline.

3. W-band radar characteristics

The primary datasets used for this study were collected with the UMass W-band radar. As mentioned above, the very narrow beamwidth of 0.18° permitted radial velocity measurements with high spatial resolution. Consequently, at a range of 1 km from the radar, the effective footprint was approximately 3 m wide. Because the area scanned was void of precipitation, the principal scattering source for the radiation returned to the W-band radar was most likely insects (Wilson and Schreiber 1986; Russell and Wilson 1997; Geerts and Miao 2005). Because the wavelength of the radiation transmitted by the radar was comparable to the size of the targets, Mie scattering was the dominant source of returned power. The minimum detectable signal for the W-band radar was -35 dBZ_e at a range of 1 km from the radar. The average reflectivity in convergence zones at this range (shown later) was about -20 dBZ_e , representing a returned power over 30 times the minimum detectable signal.

The following three scanning strategies were utilized in the 22 May case study:

- 1) Vertical antenna—antenna pointed at 86° (maximum

elevation allowed by the positioner) and driven across the boundary. The resulting time series of vertical velocity data were corrected for vehicle motion and converted to a spatial profile using recorded GPS data.

- 2) Stationary RHI (SRHI)—stationary data collection in which the antenna was rotated from approximately 0° to 86° in elevation. Multiple vertical sectors of radial velocity data were obtained in this manner. Although useful for tracking reflectivity and diagnosing radial velocity, the u and w components could not be retrieved independently with such a collection strategy.

- 3) Rolling RHI (RRHI)— 0° – 86° RHIs collected with the radar platform in motion. The radial velocity was adjusted for platform motion. The principles of pseudo-dual-Doppler analysis (e.g., Hildebrand et al. 1996) could be applied to data taken in such a manner to retrieve the individual u and w wind components (described in section 5).

4. Analysis of vertical antenna scans across the dryline

From 2221 to 2235 UTC, the UMass W-band radar executed a westward-moving vertical antenna deployment across the double dryline along U.S. Highway 270 near Elmwood, Oklahoma, in the Oklahoma Panhandle (Fig. 5). The objective of this deployment was to obtain a time series of vertical velocity in the near-dryline environment. The vehicle maintained a nearly constant speed of 27 m s^{-1} during the traverse.

The Shared Mobile Atmospheric Research and Training Radar (SMART-R; Fig. 2c; Biggerstaff et al. 2005) and SPOL (Fig. 3a) both detected a fineline associated with the eastern DCZ. This boundary was oriented in a north-northeast to south-southwest direction. Therefore, the traverses were not precisely normal, but rather

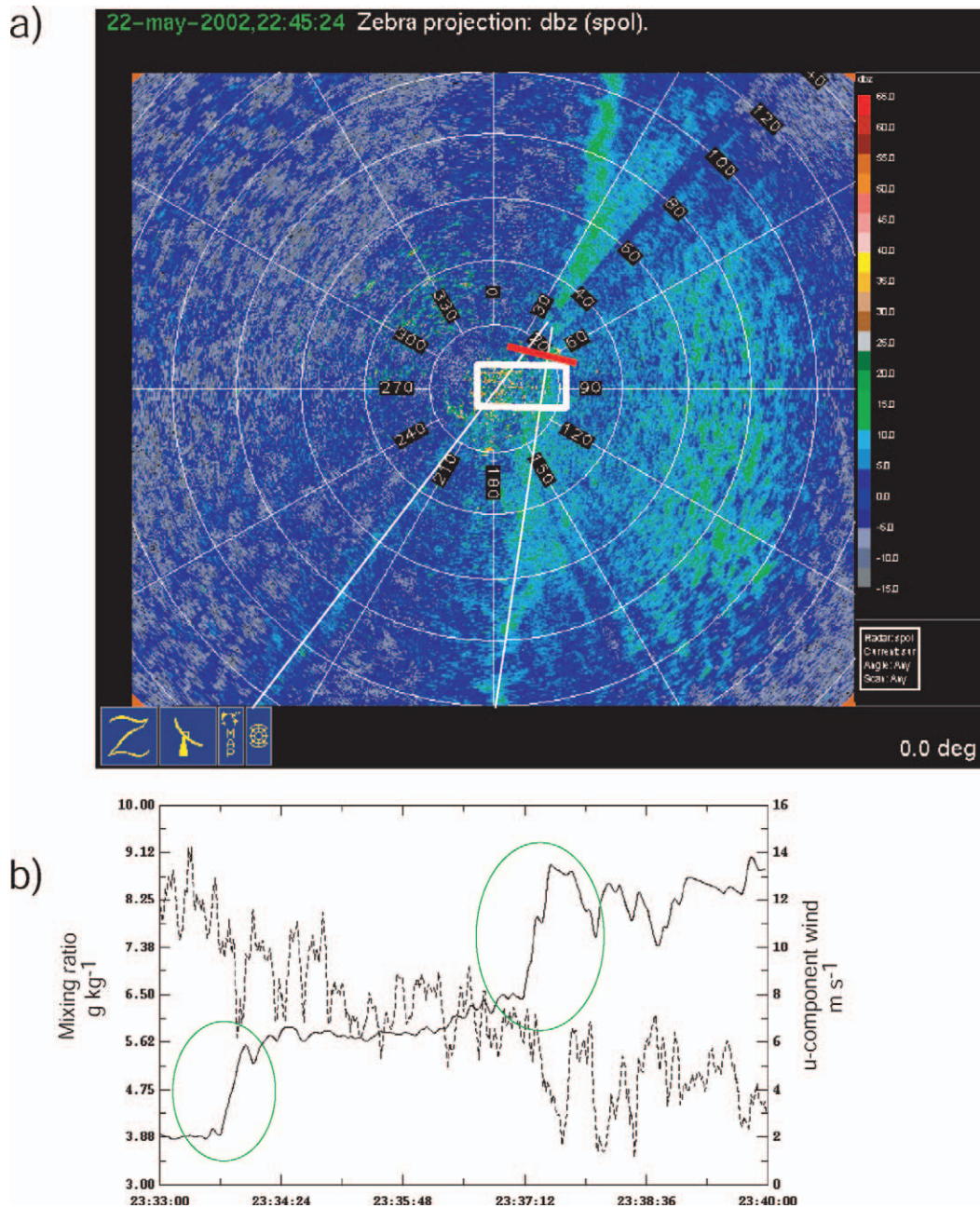


FIG. 3. (a) Reflectivity from SPOL (location indicated in Fig. 4). Reflectivity scale (dBZ) indicated to the right. The straight white lines indicate the axes of two separate drylines. The white box represents the domain of operations for the UMass W-band radar. The red line denotes the flight track of UWKA during 2333–2340 UTC. (b) Traces of in situ specific humidity (g kg^{-1} , solid trace) and u -component wind (m s^{-1} ; dashed trace) taken aboard the UWKA for the flight leg indicated in (a). Time (UTC) is indicated along the bottom axis; scales for specific humidity and u -component wind are indicated on the left and right axes, respectively. The two regions of sharp moisture gradient are circled in green.

formed a small angle from normal to the boundary. A secondary, less distinct fineline was evident to the west of the eastern (i.e., targeted) dryline. Though the western dryline was not recognized at the time of data collection, the UMass W-band radar transected this secondary feature just before the termination of the ver-

tical-antenna data collection leg (Fig. 2c). Both finelines were collocated with a specific humidity change of 2–2.5 g kg^{-1} over a distance of approximately 1 km (Fig. 3b) at the UWKA flight level (~ 800 m AGL), thereby confirming that the identified reflectivity finelines were indeed drylines.

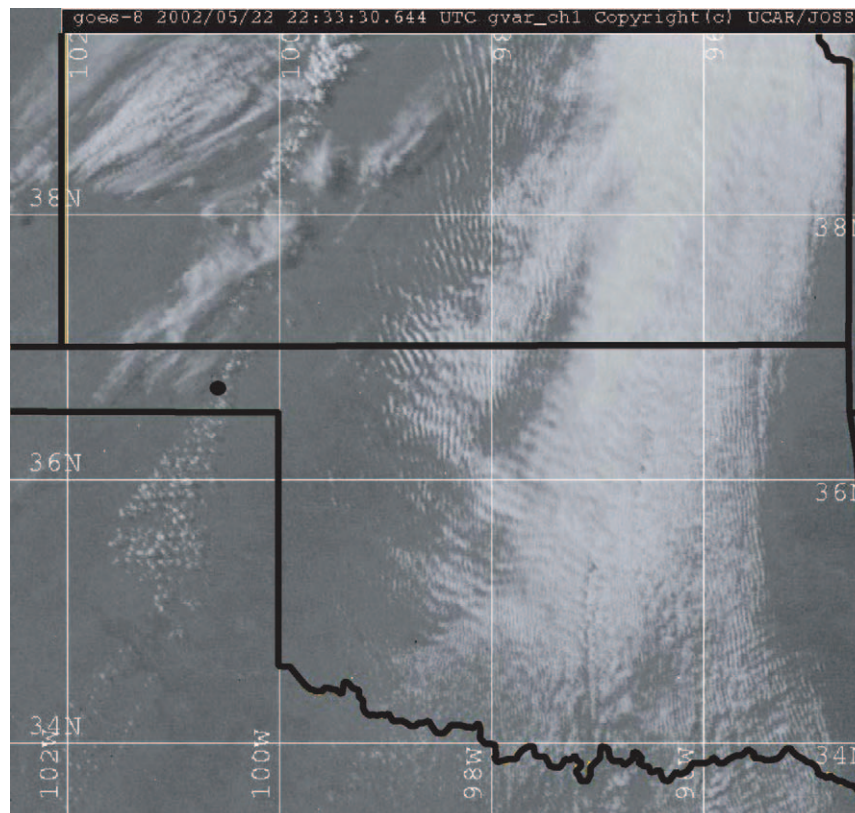


FIG. 4. Geostationary Operational Environmental Satellite (GOES-8) visible satellite image at 2233 UTC 22 May 2002. Black boundaries denote the state borders. The black dot indicates the location of SPOL.

Both drylines backscattered a detectable signal toward the UMass radar. The time section of reflectivity for this data leg (Fig. 6) shows both drylines clearly as a maximum in reflectivity. The eastern dryline returned a signal in excess of -15 dBZ_e, while the western dryline returned less power (a maximum of approximately -20 dBZ_e). The reflectivity maxima were associated with a local concentration of boundary layer scatterers that are thought to be composed primarily of insects (Wilson and Schreiber 1986). These insects are assumed to be passive, and therefore their motion is identical to that of their advecting velocity. Convergent regions like those shown in Fig. 6 accumulate these insects and therefore are more reflective (assuming the insect size distribution is the same everywhere). The relatively lower reflectivity of the western dryline in UMass and SMART-R data was presumably caused by a decreased insect concentration, either due to weaker convergence and/or a more limited source of insects.

There was a nearly vertical slope to both drylines in the lowest 1–1.5 km AGL (Fig. 6), consistent with previous observations of the forward-propagating dryline (e.g., Hane et al. 1997). Above the depth of the convective boundary layer (CBL) to the east of dryline (~ 1.5 km AGL for the eastern dryline; ~ 2 km AGL for the western dryline), the drylines tilted significantly

with height to the east (Fig. 6). Minima in reflectivity were observed in the eastern dryline interface at approximately 1.5 km AGL (Fig. 6). One of these areas (D_1 in Fig. 6) was immediately to the east of the surface position of the eastern DCZ. The other position (D_2 in Fig. 6) was about 4 km to the east of the DCZ. Even though the UMass velocity data (Fig. 7) were limited in areas D_1 and D_2 , the fringe regions about the reflectivity-void regions indicated weak descent. Similar decreases in maximum echo altitude west of the eastern dryline (e.g., west of B and C in Figs. 6 and 7) were clearly correlated with the bodies of downdrafts. Because the source for the scatterers (i.e., insects) is the surface, the scatterer concentration is nearly zero at higher altitudes (e.g., above the boundary layer). Therefore, downward motion across the dryline interface represents transport from a region where there is a dearth of insects and is therefore associated with a lack of radar reflectivity (Geerts and Miao 2005).

Observations from the WCR were considered to confirm the regions of suspected descent, and for general intercomparison with the UMass W-band radar. The WCR is an airborne W-band radar with smaller antennas, each therefore with a larger beamwidth than that of the UMass W-band radar. The flight leg (Fig. 5) crossed directly over the path of the UMass W-band

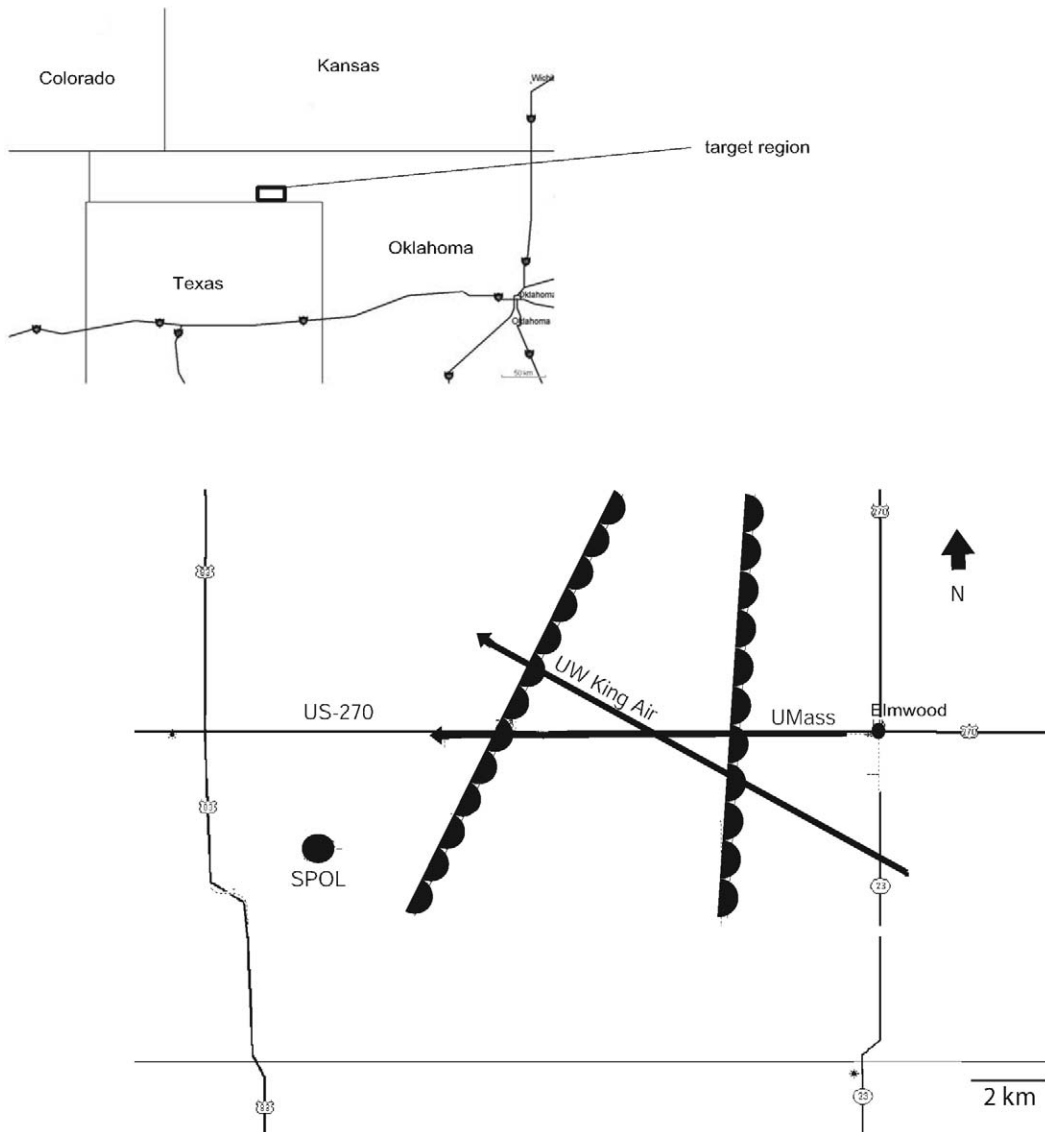


FIG. 5. Maps depicting the vertical antenna UMass W-band deployment. Distance scale located in the lower right-hand corner of the zoomed-in map. The thick lines denote the path of the UMass vertical antenna deployment from right to left (east to west) and the path of the UWKA from right to left (east-southeast to west-northwest). The scalloped lines indicate the position of known drylines. The dot labeled SPOL denotes the position of the SPOL radar near Homestead.

radar and ended approximately 10 min before the completion of the UMass data collection. The flight leg was flown normal to the eastern dryline and therefore formed an angle to the UMass ground leg. The UWKA confirmed downward motion in the suspected subsiding regions D_1 and D_2 (Fig. 8a) marked by reflectivity voids to the east of the eastern DCZ in Fig. 6. A sharp decrease in maximum echo altitude of nearly 1 km is noted by both the UMass and WCR platforms at position D_2 (consider data from 2.0 km AGL at position D_1 and from 1.5 km AGL at position D_2 in Figs. 7 and 8a).

The region of subsiding air approximately 4 km to the east of the dryline (D_2 in Figs. 8a and 8b) was ~ 3 km wide. Local vertical velocity maxima in excess of

-4 m s^{-1} were observed in this corridor. Though impossible to reconstruct trajectories from these snapshots, UMass and WCR velocity data both confirm that the subsidence extended downward from the CBL top to at least 1 km AGL. The position of this descending air was consistent with that found in the airborne radar study of Weiss and Bluestein (2002). The lowered maximum altitude of returned power in this region (~ 1 km AGL) suggested that the source region for this downward-moving air was at least in part from above the insect-rich CBL. One can therefore infer that this air had somewhat lower specific humidity. In situ measurements taken aboard the UWKA at 700 m AGL (Fig. 8c) confirm a small local decrease in dewpoint below

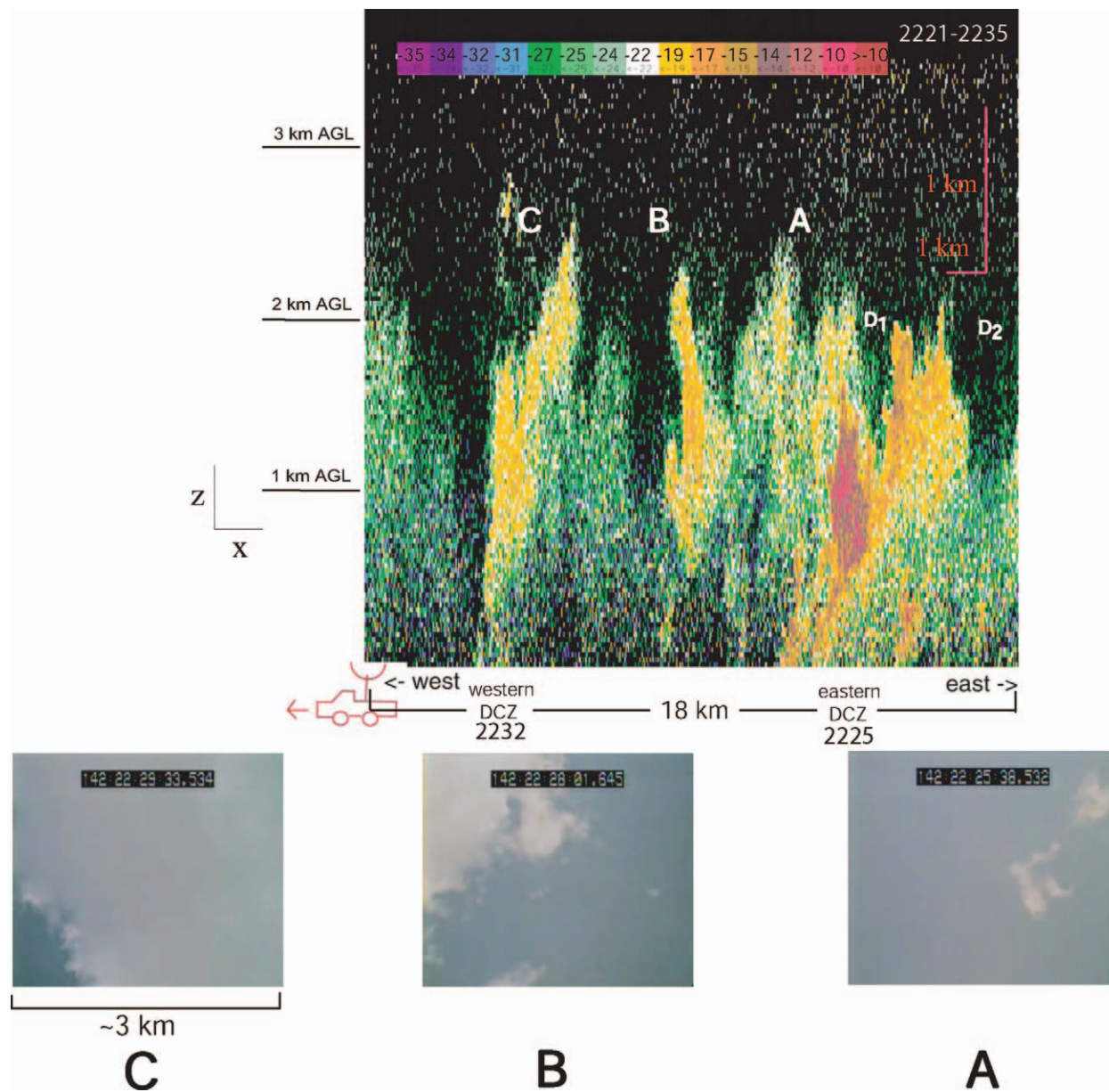


FIG. 6. East–west cross section of reflectivity from the vertical antenna deployment. Reflectivity scale (dBZ_e) is shown at the top. The 1-km scales for the horizontal and vertical direction are shown in the upper right-hand corner. Domain size is approximately 18 km wide (east–west) \times 3.4 km high. Letters A, B, and C are the locations of cloud cover discussed in the text. The UMass vehicle was in motion toward the west (left). Labels D₁ and D₂ are referred to in the text. Images of video from the W-band boresighted video camera are shown. The time of dryline passage is indicated below where the eastern and western DCZ were crossed.

the evidence of strongest subsidence. Flight-level equivalent potential temperature drops of 2 K and gust-probe-measured downward vertical velocity of 1–2 m s⁻¹ supported the assertion that subsidence was present. We speculate that these elevated regions of descent to the east of this stationary dryline may be microcosms of a larger CBL-scale process for the forward-propagating dryline, where the downward transport of low specific humidity air from above the CBL to the surface may be one mechanism to propagate the dryline eastward

(e.g., through the late morning and early afternoon hours).

UMass W-band measurements of the eastern DCZ indicated a maximum upward vertical velocity of approximately 8 m s⁻¹ (Fig. 7). However, the most intense upward motion was evident only over a very narrow region approximately 50–100 m wide. The WCR also sensed strong upward motion, with a maximum w of 6.2 m s⁻¹ (Fig. 8a). Although there were small differences in the exact location where the eastern DCZ was

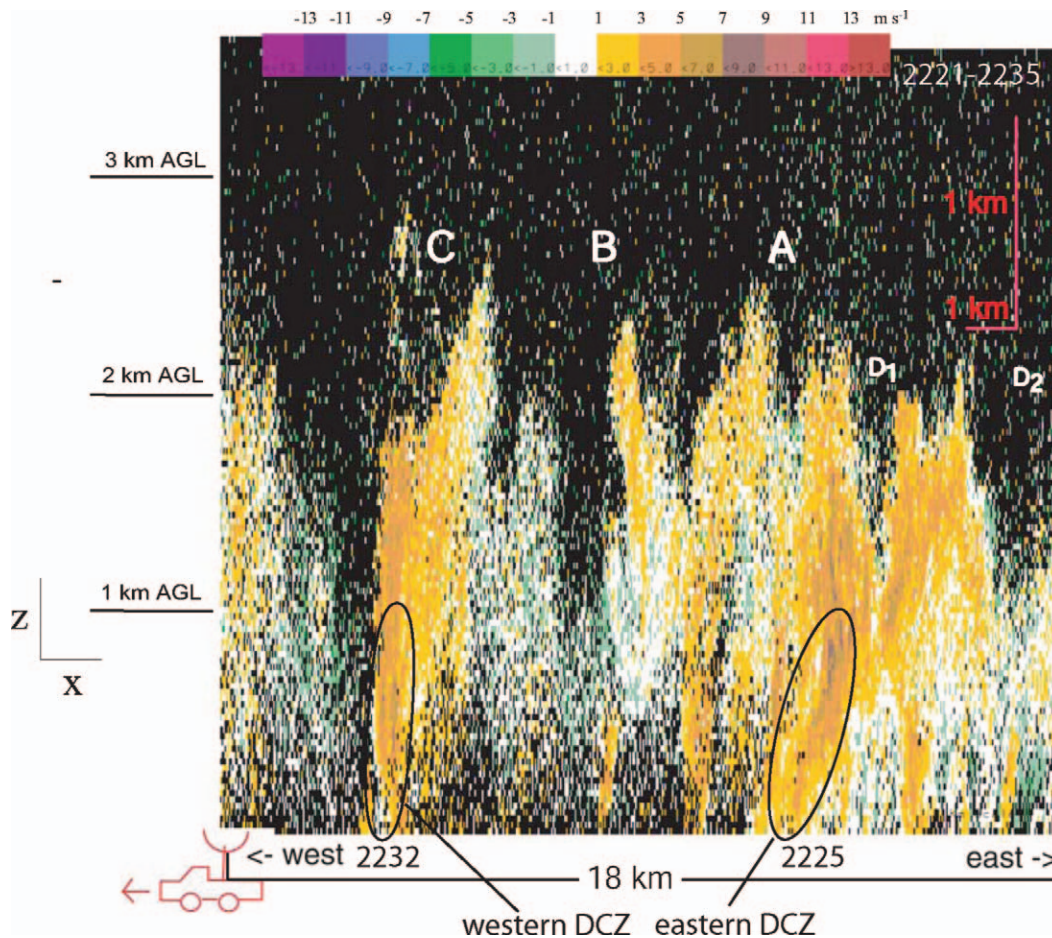


FIG. 7. Same as in Fig. 6, but the colors denote vertical velocity (m s^{-1}). Orange colors indicate upward motion; green colors indicate downward motion. Velocity scale is indicated at the top. Labels D_1 and D_2 are referred to in the text. The lower portions of the eastern and western DCZ are denoted by ovals.

crossed between the ground and flight tracks (Fig. 5), the difference in maximum w was at least partly attributable to the larger beamwidth (UMass: 0.18° ; WCR: 0.7°) and faster cross-track platform motion (UMass: 26.8 m s^{-1} ; UWKA/WCR: approximately $80\text{--}85 \text{ m s}^{-1}$) (LeMone et al. 2007). Both of these factors ultimately increased the size of the resolution volume for the WCR compared with UMass, though the faster WCR platform velocity allowed for timelier dryline sampling.

Both the UMass and WCR detected upward vertical velocity associated with the convergence zone of the western dryline. The WCR indicated a maximum ascent of approximately $3\text{--}4 \text{ m s}^{-1}$ (Fig. 8a), while UMass measured a maximum w of $\sim 5 \text{ m s}^{-1}$ in narrow regions (Fig. 7). Again, the effective beamwidth may have contributed to this difference. Also, the difference in slope and decreased distance between the eastern and western drylines³ (compared with observations from the UMass

radar) suggest that the WCR measurements may have been made on a distinctly different portion of the western dryline. Regardless, it is seen in data from both platforms that there was a wide region of descent approximately $3\text{--}4 \text{ km}$ wide centered about $4\text{--}5 \text{ km}$ east of the western dryline. A decrease in dewpoint of 1°C was seen here as well as in UWKA in situ data (Fig. 8c).

Reflectivity data from SPOL (not shown) indicated that the eastern dryline had begun to retrograde at approximately 2230 UTC. WCR data from two passes centered around 2230 UTC (nearly identical in position; separated by $\sim 25 \text{ min}$) reveal a widening of the distance between the two drylines, suggesting a different retrogression speed and/or onset for each dryline. Furthermore, the easternmost dryline had established a much more pronounced eastward tilt with height in the second WCR pass. The inclined slope of the interface appears qualitatively similar to that observed in propagating density currents.

A boresighted video camera was mounted on the

³ Recall that the UWKA intercepted the western dryline north of the UMass intercept (Fig. 5).

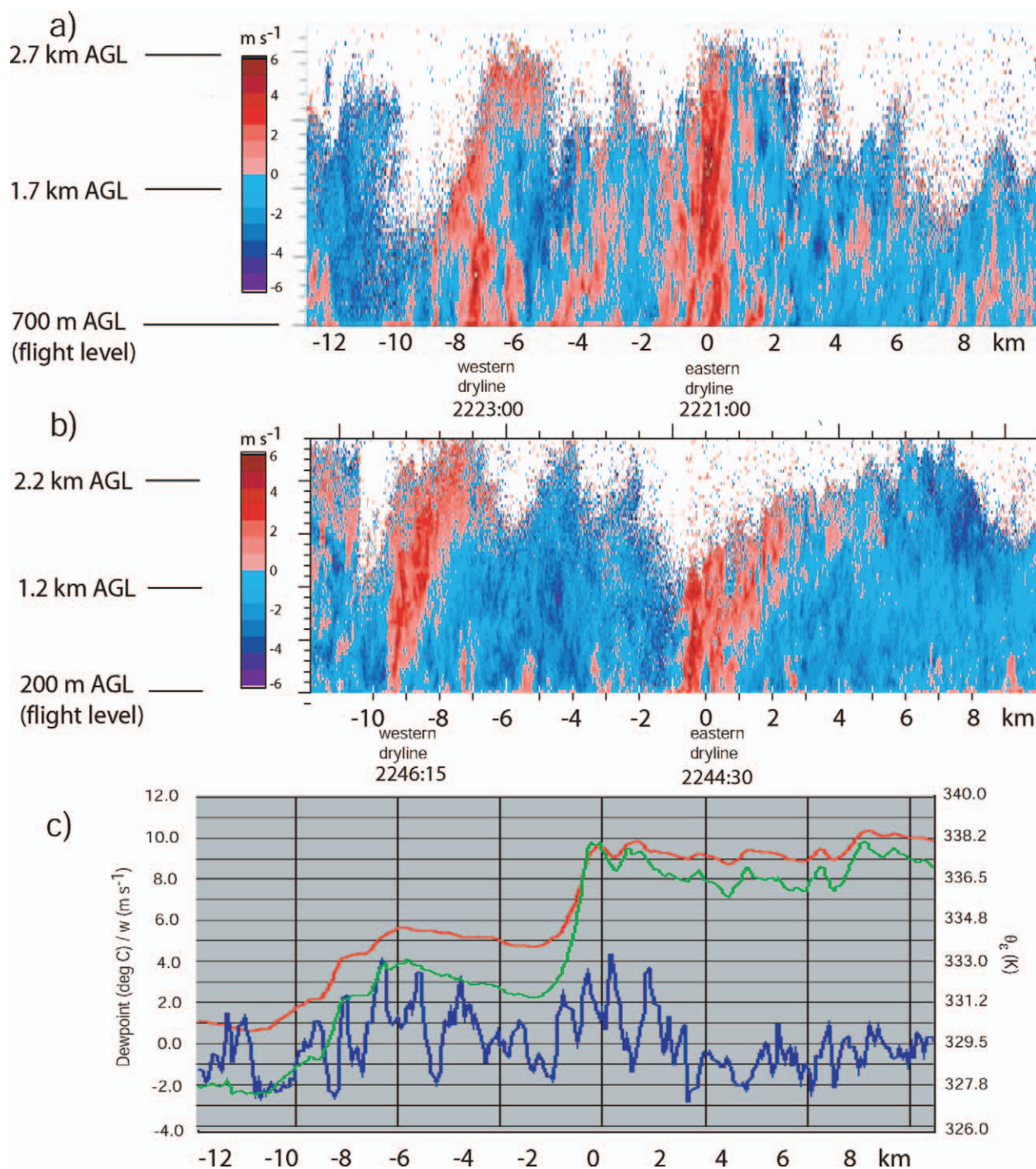


FIG. 8. WCR vertical velocity (m s^{-1} , scale to left) during (a) 2218–2224 and (b) 2241–2248 UTC. (c) Trace of in situ dewpoint (red trace; $^{\circ}\text{C}$; scale included to left), θ_e (green trace; K; scale included to right), and vertical velocity (blue trace; m s^{-1} ; scale included to left) measurements at flight level (700 m AGL) aboard the UWKA during 2218–2224 UTC. The horizontal distance scale in all three images represents the distance (km) east (positive) or west (negative) of the eastern dryline (positioned at 0 km). The vertical distance scale is in km AGL [note the different flight altitudes in (a) and (b)]. Labels D_1 and D_2 are referred to in the text.

W-band antenna to assist the radar operator (the first author) in the proper placement of the narrow beam during field operations. At times when the antenna was pointed vertically, the video served to identify regions

of cloud cover directly above the instrument. Three such regions were found during the deployment. The first area (labeled A in Figs. 6 and 7), immediately to the west of the eastern DCZ, was populated by very shallow

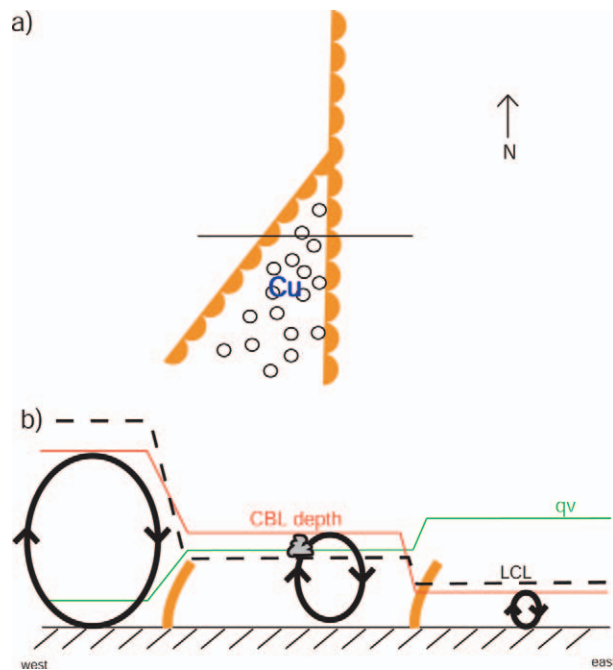


FIG. 9. A (a) plan view and (b) east–west cross section schematic of “wedge sector” cumulus. Circles in (a) denote boundary layer convection. In (b), the “qv” and “CBL depth” traces indicate the surface specific humidity and convective boundary layer depth, respectively. The dashed line denotes the location of the LCL.

cumulus clouds. The second area, likely associated with the ascending branch of a horizontal convective roll (HCR; LeMone 1973), was found halfway between the eastern and western DCZ (labeled B in Figs. 6 and 7), and contained more vigorous convection (Fig. 6). The third area of cloud cover, by far the widest (~ 2 km), was associated with the DCZ of the western dryline (labeled “C” in Figs. 6 and 7). No cumulus cloud field was seen outside the intermediate region between the drylines.⁴ This observation was consistent with the “wedge” shape of cumulus convection seen on satellite images (Fig. 4).

It is hypothesized here that the wedge zone represented an optimal combination (for boundary layer cumulus development) of the highest specific humidity to the east of the eastern dryline and the deepest CBL to the west of the western dryline (Fig. 9). Signal-to-noise ratio (SNR) data (Fig. 10a) from the NCAR Integrated Sounding System (ISS)/Multiple Antenna Profiler Radar (MAPR; Cohn et al. 2001) indicated a rapid increase in the boundary layer depth to 3.5–4.0 km AGL (considering the altitude of the 0-dB SNR surface) by 2200 UTC as the Homestead profiling site sampled the wedge region (Demoz et al. 2006). Upward vertical velocity was evident through this boundary layer depth (Fig. 10b), supporting the notion that surface-based air parcels were freely ascending to this level. Remotely-

⁴ A narrow band of cirrus clouds, however, was seen.

sensed soundings from the Atmospheric Emitted Radiance Interferometer (AERI; Feltz et al. 2003) in the wedge region at 2158 UTC confirm a level of free convection (LFC) height of approximately 2.7 km (4.0 km) (Fig. 11a). Considering the depth of the convective ascent noted by the MAPR, it is clear that lifted condensation level (LCL) was reached easily in the wedge region. Another AERI sounding taken at 0013 UTC (Fig. 11b), after the eastern dryline retreated westward through the profiling site, reveals the expected lowering of the LCL (to approximately 2.1 km AGL). MAPR data near the same time indicate a boundary layer depth (again, using the 0-dB SNR surface) of 1.8–2.4 km. With relatively weak upward velocity detected (compared to the wedge region) in the boundary layer, these findings largely confirm the visual observation that the LCL was not reached to the east of the eastern dryline. As the western dryline did not propagate through the profiling site, no MAPR information is available to confirm the depth of the boundary layer in the dry air. However, UWKA in situ data (Fig. 3b) and surface observations (Fig. 1) do identify another sharp decrease in moisture in association with the western dryline, likely limiting cumulus development.

5. The variational analysis of rolling RHI data

a. Motivation and technique development

One goal of this study was to synthesize, with radial velocity from a single radar, the secondary circulation normal to the plane of the dryline. In general, a time series of stationary RHIs are often used to capture the vertical evolution of atmospheric boundaries. With this technique, the individual components of motion in the plane of the RHI cannot be retrieved without making assumptions about one of the components (e.g., w is constant over the domain).

If the platform is in motion during the collection of the RHIs (the RRHI technique), then the two components of motion can be retrieved using pseudo-dual-Doppler principles (Hildebrand et al. 1996). An arbitrary point in space will be seen a number of times from varying “look” angles using such a strategy (Fig. 12). An assumption inherent to this technique is that of *stationarity*—that nothing varies at the point over the time elapsed between the “looks.” One can expect this assumption to be more valid for larger scales of motion with limited translation.

Because a substantial number of overlapping radial velocity measurements were made using the RRHI scanning strategy, an analysis technique had to be developed to accommodate the overdetermined system. For this study, a weak-constraint variational (Sasaki 1970) wind synthesis technique was developed for rolling RHI data taken in an east–west plane. A cost function is defined that is a function of the dependent analysis variables. The cost function (J) penalizes the analysis for depar-

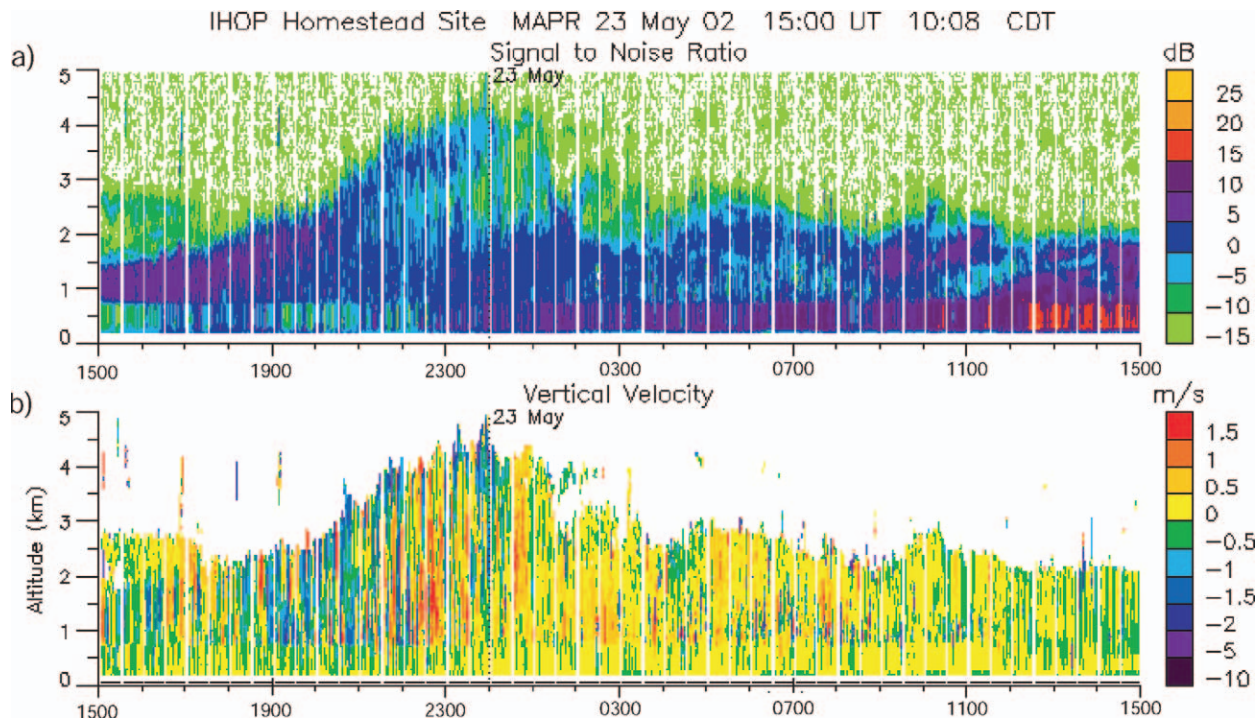


FIG. 10. (a) SNR (dB) and (b) vertical velocity (m s^{-1}) data from the MAPR, positioned at Homestead. The data in the display are valid from 1500 UTC 22 May 2002 to 1500 UTC 23 May 2002.

tures from radial-velocity observations and kinematic or dynamic constraints. The cost function chosen to be minimized for this case was

$$J = \sum_{\text{domain}} (J_{\text{obs}} + \beta J_{\text{continuity}}) \quad (1a)$$

$$J_{\text{obs}} = \sum_{n=1}^{m(x,z)} (c_1^n u + c_2^n w - \mathbf{V}_r^n)^2, \quad (1b)$$

$$J_{\text{continuity}} = \left(\frac{\partial u}{\partial x} + \frac{\partial w}{\partial z} + \kappa w \right)^2, \quad (1c)$$

$$c_1^n = \cos(\alpha^n), \quad \text{and} \quad (1d)$$

$$c_2^n = \sin(\alpha^n), \quad (1e)$$

where Eq. (1b) represents the contribution to the cost function from observational discrepancy and Eq. (1c) denotes the contribution to the cost function from anelastic mass continuity violation. In Eqs. (1a)–(1e) u and w are the analysis values, \mathbf{V}_r is the observed radial velocity (corrected for platform motion), c_1 and c_2 represent geometric coefficients mapping velocities from Cartesian space to that of the radial velocity vectors, κ is the correction to mass continuity for vertical density stratification (assumed constant here), m is the total number of observations per grid point of which n is a specific observation, and α is the elevation angle for each observation. The parameter β represents the relative impact of departures from radial velocity observations and violation of mass continuity in the calculation of J . For the analyses presented below, β was

constant and set proportional to the square of the grid spacing $[(\Delta x)^2]$. The formulation was similar to that developed by Gao et al. (1999) (less a background and smoothness constraint) and Dowell and Bluestein (2002) (neglecting variations in the y direction).

The variations of J with respect to u and w were set equal to zero, yielding two coupled Euler–Lagrange equations (not shown). The two equations were repeatedly solved in turn until the solutions for u and w over the entire domain converged.

b. Testing

A series of observational system simulation experiments (OSSEs) was created to examine the behavior of the variational synthesis technique presented. Specifically, it was desired to elucidate the relation between analysis error and scanning strategy. To this end, a prescribed constant flow field of $u = 10 \text{ m s}^{-1}$ was sampled with a UMass “pseudoradar.”⁵ The platform velocity was due westward, and the scanning plane was oriented east–west. The platform velocity and vertical antenna rotation rate (hereafter, scan rate) were allowed to vary. Data were “stored” at a frequency of 10 Hz, matching the specifications of the signal processor in the UMass

⁵ The synthesis procedure also tested successfully with OSSEs derived from large-eddy simulation (LES) output, where large gradients in the horizontal and vertical wind components were present (not shown).

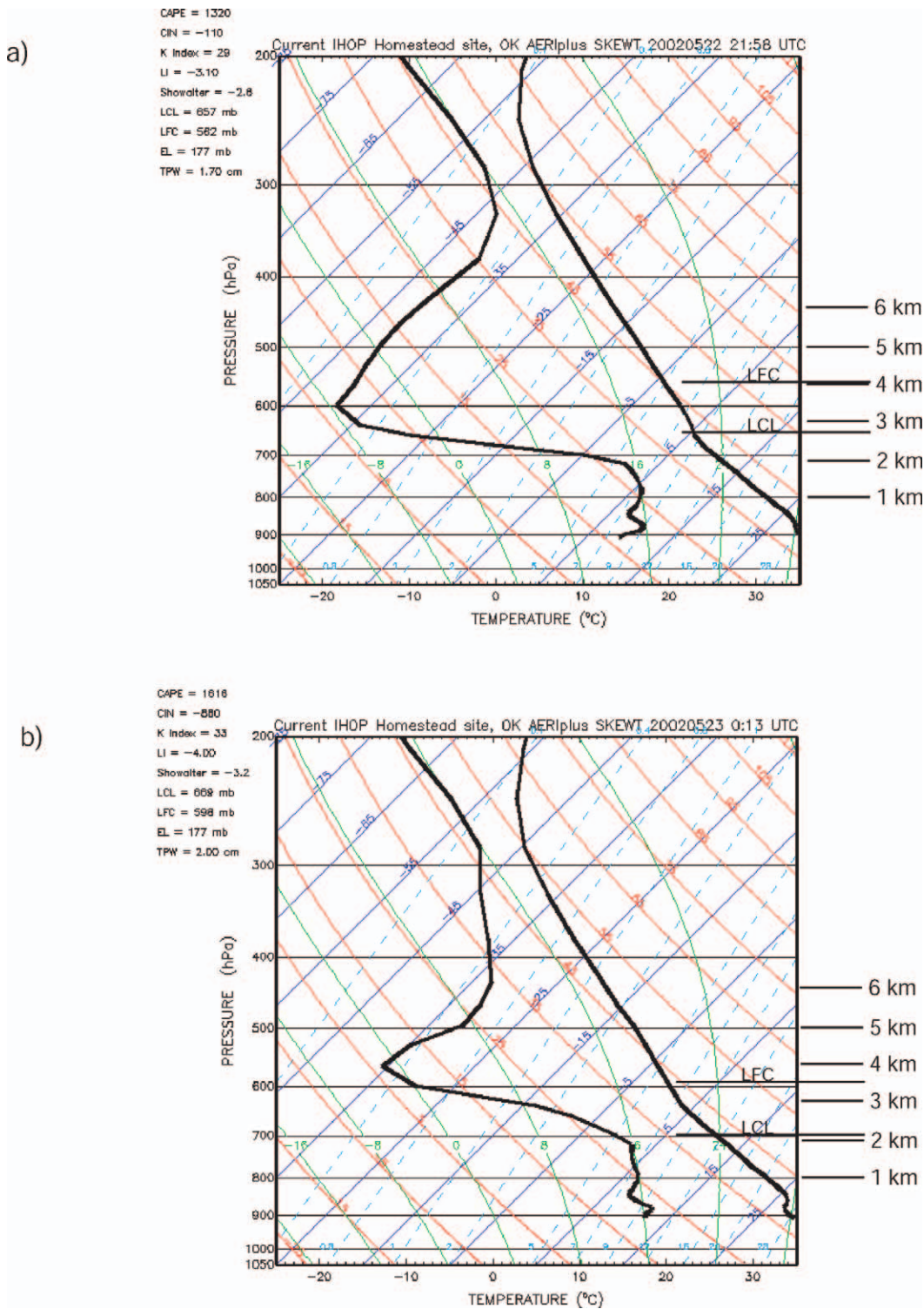


FIG. 11. AERI-derived soundings from the Homestead profiling site valid at (a) 2158 and (b) 0013 UTC. Height (km AGL), LCL, and LFC are identified to the right of each panel.

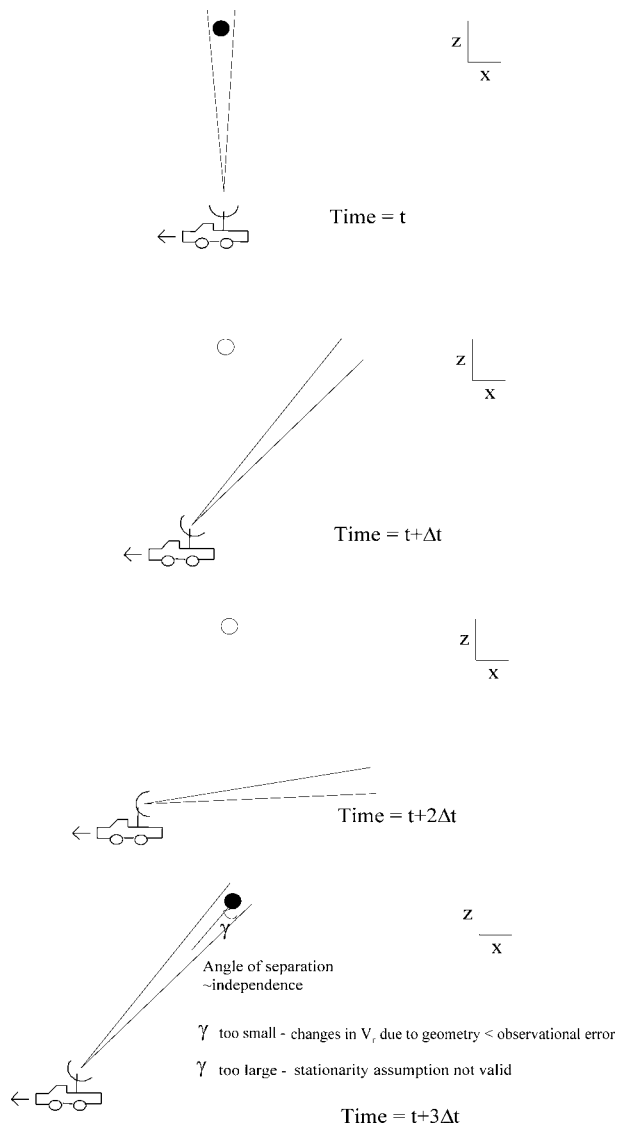


FIG. 12. Schematic of RRHI method of data collection. The circle aloft represents a fixed arbitrary resolution volume during (filled) and in between sampling (open).

W-band system. In all cases, a first guess field of no flow ($u = w = 0$) was used.

Initial simulations were performed with a platform velocity of 15 m s^{-1} and a scan rate of 1.5° s^{-1} —scanning parameters identical to that of the IHOP data collection on 22 May 2002. The u -component analysis winds verified very well against the truth field (Fig. 13a), with a domain total RMS error of 0.10 m s^{-1} . It is noted that almost all of the error accrued in periodic minima in u along the upper portion of the domain. It is in this region that the difference in viewing angle amongst the looks (hereafter, the look angle difference) was small.

Observational error is a natural consequence of any radar platform. These errors can vary in origin (e.g.,

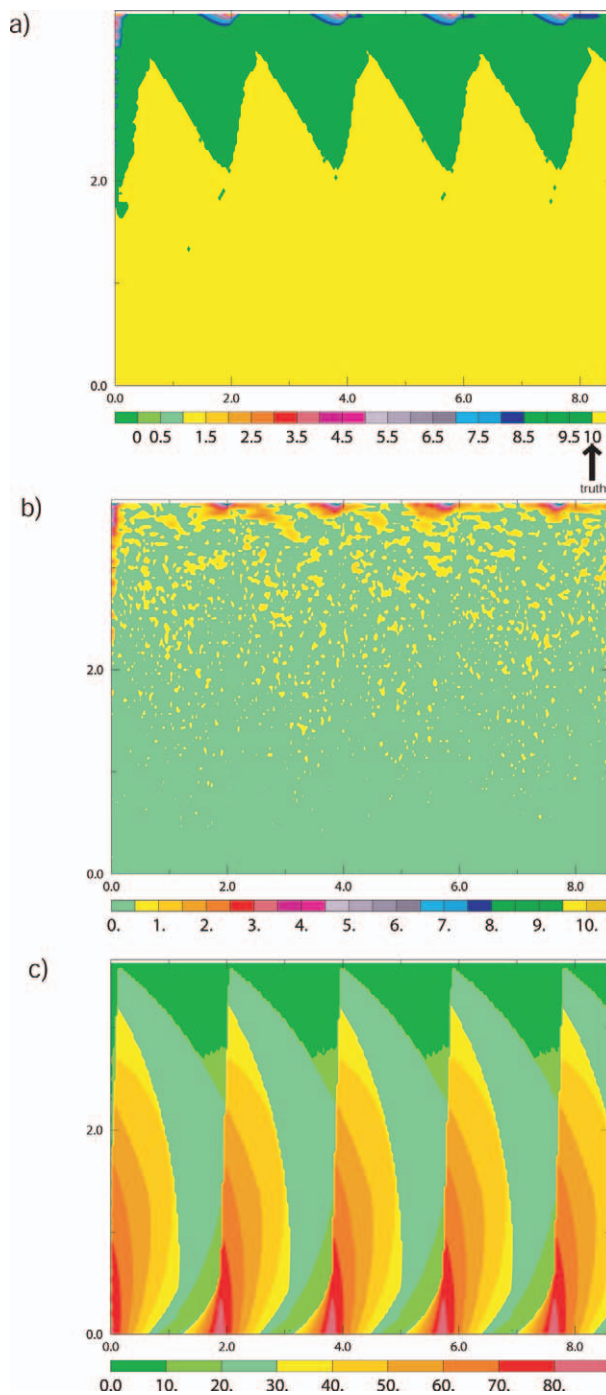


FIG. 13. (a) The u -component wind velocity (shaded; m s^{-1}) from a homogeneous-flow OSSE with a platform velocity of 15 m s^{-1} , a scan rate of 1.5° s^{-1} , and no observational error. (b) The u -component absolute wind velocity error (shaded; m s^{-1}) from the same OSSE as in (a), but with an imposed observation error standard deviation of 1.0 m s^{-1} . (c) Maximum look angle difference (shaded; degrees) for the analyses in (a) and (b). Distance labels (km) are provided on each axis.

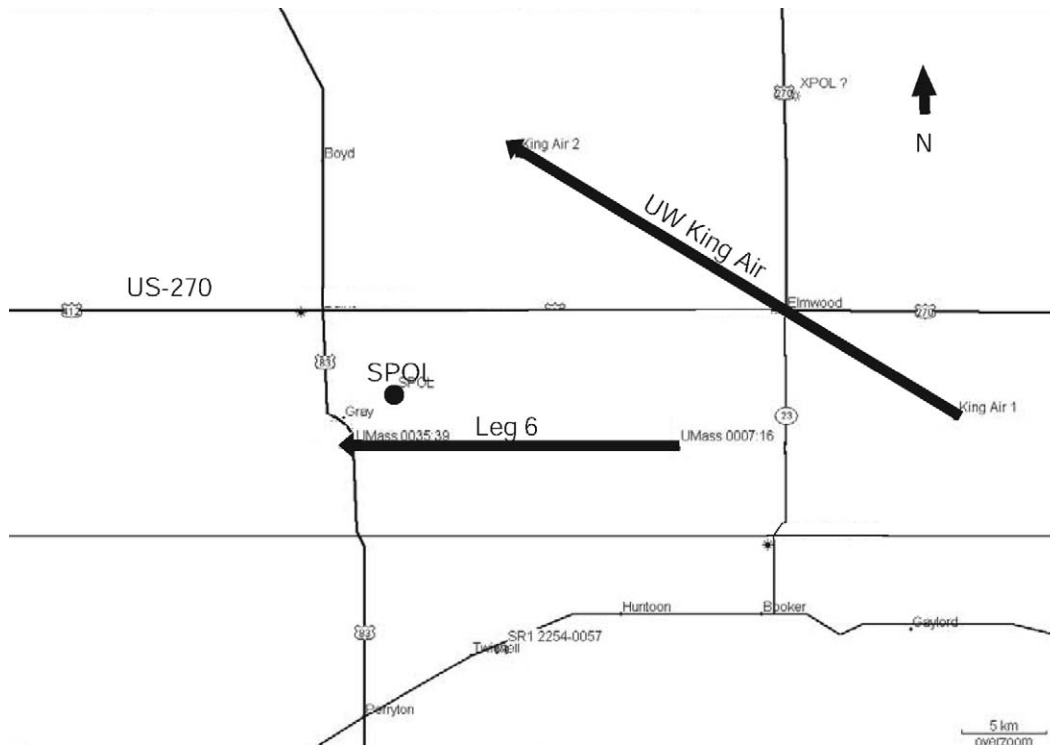


FIG. 14. A map of the rolling RHI UMass W-band deployment (0007–0036 UTC). Distance scale located in the lower-right-hand corner. The thick lines denote the path of the UMass rolling RHI deployment from right to left (east to west), and the path of the UWKA (2345–2351 UTC) from right to left (east-southeast to west-northwest). The dot labeled SPOL denotes the position of the SPOL radar at Homestead.

system noise, sidelobe contamination, anomalous propagation, and beam spreading). To simulate this effect, Gaussian (i.e., random and normal) errors were added to the time series of radial velocity data obtained with the pseudoradar. To mimic the error characteristics of the UMass radar, the standard deviation of the applied error was 1.0 m s^{-1} . These imperfect data were then processed in the same manner as above. The synthesis technique continued to perform very well (Fig. 13b), with an analysis RMS error of 0.379 m s^{-1} . Much like the observation-error-free case, the largest errors were contained in the upper portion of the domain, where maximum look angle differences were subcritical. Since the analysis was biased toward the first-guess values in these areas, an evident underapplication of the observation increments occurred in these locations. Consistent with this conclusion, an analysis error equal and the opposite in magnitude was found if the first guess was changed to $u = 20 \text{ m s}^{-1}$.

The OSSEs confirm that, given a time series of rolling RHI data, the variational synthesis technique provides an accurate depiction of the true two-dimensional flow, if a sufficient amount of independence (i.e., large look angle difference) exists amongst the observations. To ensure that this condition is met, it is desirable to obtain data with as fast a scan rate as possible, taking into consideration the beamwidth and sample averaging for

the upper limit. A slower platform motion allows for more looks at any arbitrary point, which, considering the random nature of the observational error, permits a better determination of the true radial velocity. However, concerns about the stationarity assumption must be weighed against this benefit. Naturally, one cannot fully resolve temporal scales of motion faster than the time between the first and last looks. For the later looks at each grid point, in particular, the trade-off between stationarity and look angle separation becomes significant.

6. Analysis of rolling RHI scans across the dryline

During 0007–0036 UTC, the UMass W-band radar executed a westward-moving RRHI deployment across the eastern dryline (Fig. 14). The geometry of the RRHI scanning strategy permitted the overlap of rays (Fig. 15) and therefore was compatible with the variational processing technique described above. Assuming stationarity of the wind field for the time period between the looks (discussed below), we used the technique to synthesize the u and w wind components in the plane approximately normal to the dryline.

The dryline was beginning its nocturnal retrogression as the RRHI data were being collected (Fig. 16). The retrogression was not uniform along the dryline as evidenced by the change in the radar fineline location,

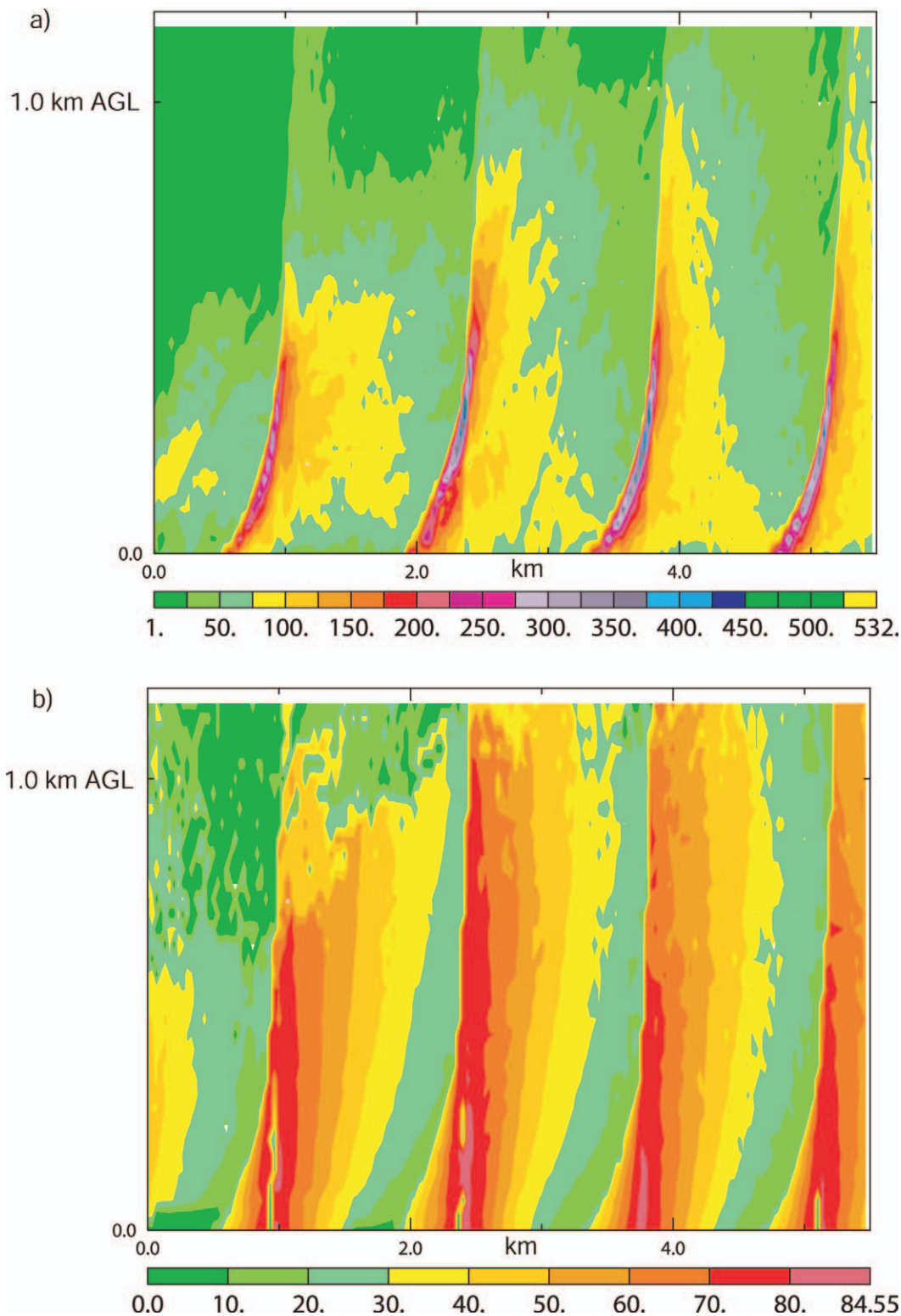


FIG. 15. (a) Look count and (b) maximum look angle difference (degrees) for the 22 May 2002 dryline analyses with no data window cutoff imposed (discussed in text).

220

METEOROLOGICAL MONOGRAPHS

Vol. 33, No. 55

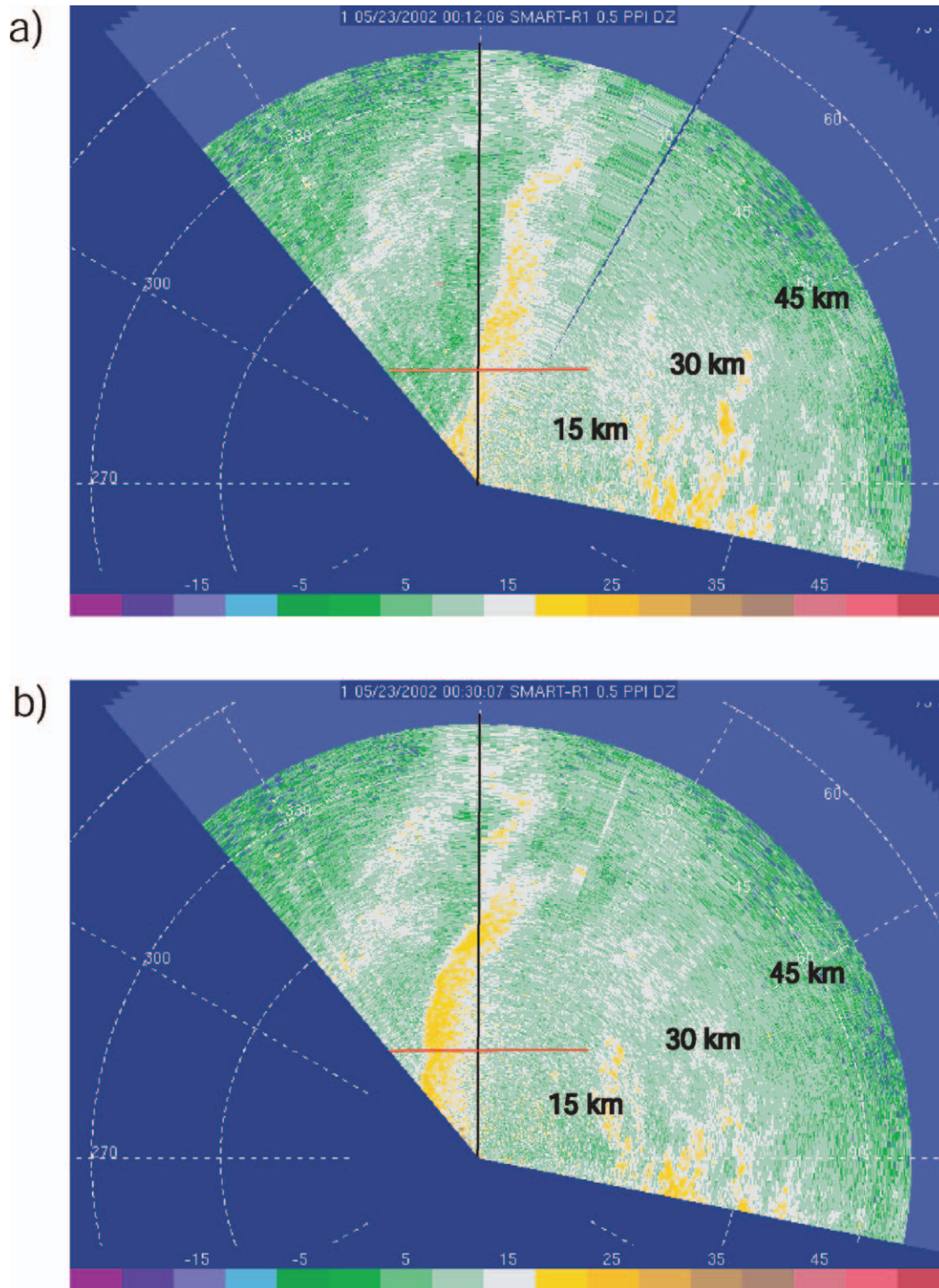


FIG. 16. SMART-R 0.5° reflectivity (dBZ) valid at (a) 0012 and (b) 0030 UTC. The north radial is highlighted in black to show retrogression more clearly. The approximate path of the UMass rolling RHI (right to left) is shown in red. Range markers are indicated in black.

since there was evidence of wave activity along the dryline interface. Data from various radar platforms permitted an estimated retrogression speed between 2 and 5 m s^{-1} during the period of the traverse. The motion

of the dryline and evident heterogeneities in dryline position upwind of the analysis plane made the stationarity assumption more restrictive; therefore, for each point in the analysis domain, a data cutoff window of

60 s (from first observation) was introduced. This window size appeared to balance best the concerns of stationarity (for a window too large) and observations that were too dependent (for a window too small). Reduced total look counts and maximum look angle differences were a natural consequence of the imposed data window (Fig. 17). The UMass radar platform traveled at a nearly constant velocity of 13 m s^{-1} toward the west as RHI sweeps were taken (with a scan rate of 1.5 degrees per second) from the rear horizon up through $\sim 86^\circ$ above the rear horizon. The raw time series of data were post-processed to account for truck velocity and pitch (using digital elevation models) before the data were analyzed.

In a composite reflectivity image for the traverse (Fig. 18), the pronounced eastward tilt of the dryline interface with height during retrogression can be seen. As with the vertical antenna deployment, the DCZ appeared as a maximum in reflectivity, presumably due to the local increase in insect concentration in this region. The domain chosen for analysis was the lowest 1 km AGL, where there were no data voids.

It is seen from the analyses using the variational technique that the upper and lower branches of the dryline secondary circulation were resolved quite clearly (Fig. 19a). The near-surface inflow to the DCZ from the east approached $u = -6 \text{ m s}^{-1}$ in some areas of the CBL. Near the top of the CBL, strong westerly component winds (i.e., the return flow) were evident, a combination of air parcels from the moist CBL that had ascended in the DCZ (Hane et al. 1997) and parcels from the dry side that had advected up and over the moist CBL. Westerly winds upward of $u = 15 \text{ m s}^{-1}$ were identified in this region.

The DCZ showed up clearly in the w -component field (Fig. 19b) as a maximum w of $8\text{--}10 \text{ m s}^{-1}$. As with the stationary dryline earlier (section 4), the channel of maximum vertical velocity was only $\sim 100 \text{ m}$ wide. The eastward tilt of the DCZ with height was again present, much more so than with the stationary dryline. A small area of descent was evident at $\sim 500 \text{ m}$ AGL approximately 3 km to the east of the surface position of the DCZ (labeled “D” in Fig. 19b). The position of this descending motion was similar to that shown for the vertical antenna deployment earlier and the airborne Doppler case study of Weiss and Bluestein (2002), both stationary dryline cases.

To examine the effect of the β parameter [Eq. (1a)] on the analysis, the value of β at each point was multiplied by the number of looks at that point. The influence of the mass continuity constraint in the analysis was consequently increased, producing the smoother field depicted in Fig. 20. One can still see very clearly the discontinuity in the u -component (Fig. 20a) and w -component fields at the dryline interface (Fig. 20b) and the rotor circulation on the head of the dryline secondary circulation (DSC). From Figs. 20a and 20b it is clear that the easterly component winds at the surface

extended to the west of the area of maximum upward motion.

7. Summary and discussion

This study was driven by the desire to resolve the finescale structure of a near-dryline environment. This aim was accomplished utilizing instruments capable of high-resolution observations in clear air—the U-Mass W-band and UWKA/WCR—and by developing a pseudo-multiple-Doppler radar processing technique to decompose radial velocity vectors into the individual components of motion.

On the afternoon of 22 May 2002 during IHOP, the UMass W-band was deployed on a double dryline event in the Oklahoma Panhandle. With the antenna pointed vertically, the radar was driven westward across both dryline boundaries. The DCZ was well resolved; a maximum upward vertical velocity $w \sim 8 \text{ m s}^{-1}$ was measured in a narrow channel of the eastern DCZ, approximately $50\text{--}100 \text{ m}$ wide. In the past, details such as these were hard to discern. For example, Atkins et al. (1998) reported upward motion on the order of $1\text{--}2 \text{ m s}^{-1}$ using NCAR Electra Doppler Radar (ELDORA) data with a relatively coarse horizontal (along-track) resolution of 600 m . Parsons et al. (1991) used lidar technology (with horizontal resolution of 200 m) to measure a maximum positive vertical velocity of $w \sim 5 \text{ m s}^{-1}$ on a retrograding dryline in west Texas. The larger magnitudes of vertical velocity seen in the current study are likely in part due to the narrow beamwidth of the antenna, which reduced the cross-dryline width over which velocity discontinuities were measured in the DCZ, and allowed for measurements very near the surface without contamination from the ground. Both of these effects allowed for a more accurate determination of the magnitude and depth of convergence in the DCZ.

Areas of subsidence were noted away from the DCZ of both drylines. One such area was found in both UMass W-band and WCR data approximately $4\text{--}5 \text{ km}$ east of the eastern DCZ. This position was consistent with a similar finding by Hane et al. (1993), in which the area of descent coincided with a moisture gradient at the surface. In this case, it does not appear that the subsidence was sufficient to reach the surface. Small decreases in dewpoint and equivalent potential temperature were identified by UWKA flight-level measurements in the middle of the boundary layer in the descending regions. The areas of concentrated subsidence discussed above are potentially significant for many issues related to the dryline. Double drylines, for example, may form in such a manner, similar to that of the observations of Hane et al. (1997, 2001), and that of the modeled “microfronts” of Ziegler et al. (1995).⁶ The transport of dry air to the surface in the near-dryline

⁶ Subsidence would need to be deeper than in the current case for these features to be realized at the surface.

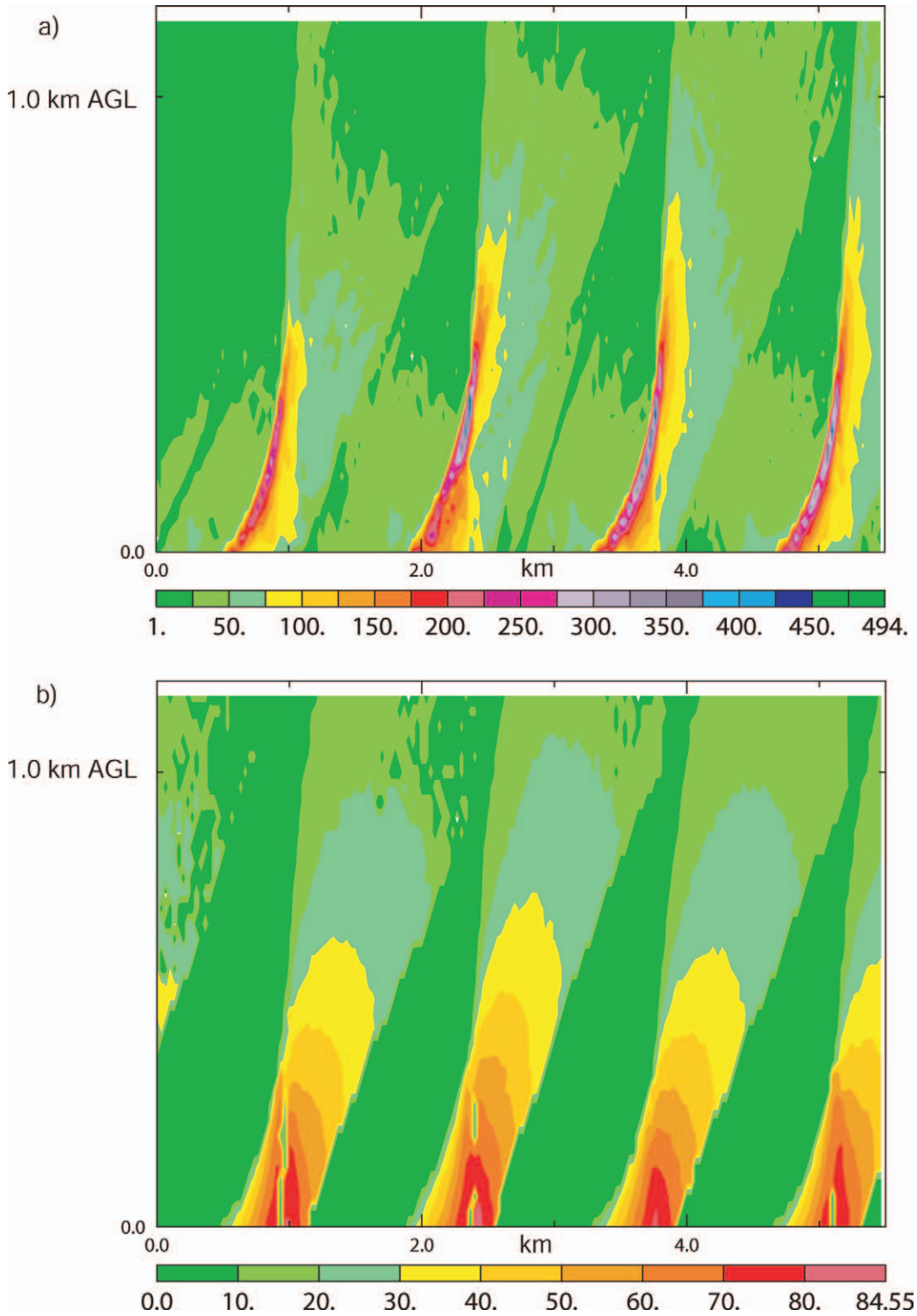


FIG. 17. (a) Look count (shaded) and (b) maximum look angle difference (shaded; degrees) for the 22 May 2002 dryline analyses (Figs. 19 and 20) with a data window cutoff of 60 s imposed (discussed in text).

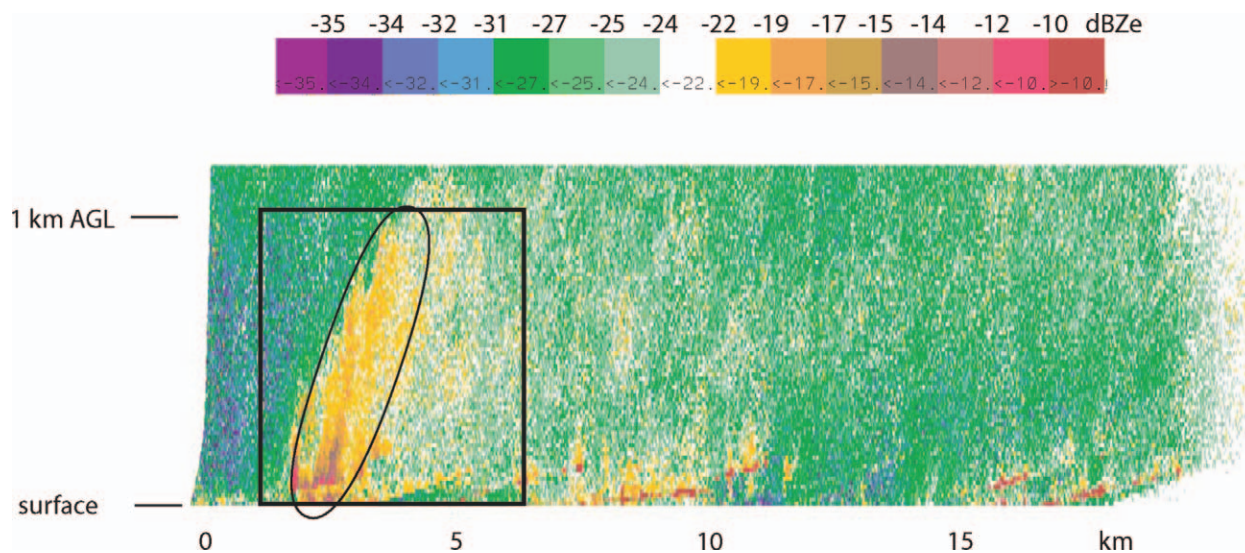


FIG. 18. An east-west display of composite reflectivity from the UMass rolling RHI (0007-0036 UTC). Horizontal and vertical distance scales are indicated. The black box denotes the domain for analysis. The black oval denotes the DCZ.

environment can have substantial effects. In a case presented by Hane et al. (1997), vertical mixing of westerly momentum down to the surface was hypothesized to form a convergence line in the dry air west of the dryline. Severe thunderstorms were later initiated at the intersection point of this convergence line and the dryline.

Data analyzed from the vertical antenna deployment also indicated descending motion immediately to the west of both drylines. This finding agrees with some recent airborne studies of the dryline (e.g., Atkins et al. 1998; Weiss and Bluestein 2002). Because this downward motion transports westerly momentum toward the surface, these observations are consistent with previous observations of westerly component acceleration immediately to the west. More data need to be gathered to assess how ubiquitous this downward motion is, and whether any skill can be realized at predicting convection initiation with these types of observations.

Later during the evening of 22 May 2002, the UMass W-band radar collected RRHI data on the eastern dryline as it retrograded toward the west. The data were analyzed using a variational pseudo-multiple-Doppler radar processing technique, developed specifically for the RRHI collection strategy. This technique was tested using simulated sets of radial velocity derived from fields of known velocity. These tests confirmed the robustness of the technique, with domainwide RMS errors well below the prescribed observational errors. The technique performs the worst when, like any pseudo-Doppler processing algorithm, the observations are close to being collinear. The analysis is biased toward the first guess in these cases.

The assumption of stationarity is central to pseudo-dual- or pseudo-multiple-Doppler data processing. The accuracy of this assumption degrades as the time be-

tween observations increases. For airborne pseudo-dual-Doppler techniques (Jorgensen et al. 1995), this elapsed time is a function of range from the aircraft. In the design presented here, areas above and to the near east (in this case) of the vertically pointed radar will have observations separated by the greatest amount of time. However, unlike the airborne dual-Doppler case, there will also be a greater number of observations and a larger separation in angle between each look—both factors that will improve the analysis at these locations. The trade-off between observation collinearity and stationarity is of great significance for practical application of this processing technique. A data cutoff window must be introduced that balances these concerns. For this case, the optimal value of the cutoff window was found to be 60 s. If the dryline were not retreating, a less-restrictive value could have been used.

The OSSEs reveal that the scan strategy used on 22 May 2002 was suboptimal. Faster scan rates would have provided more expansive multiple-Doppler lobes (i.e., regions with sufficient separations in look angle). The introduction of a data cutoff window only exacerbates the negative effects of the slow scans. However, the existing lobes were fortuitously positioned to resolve extrema in vertical velocity near the head of the retreating dryline in this study.

The variational analyses from the 22 May 2002 case depicted the legs of the dryline secondary circulation with great spatial detail. The dryline interface appeared more tilted than seen earlier in the afternoon with the stationary dryline. The rotor circulation and sloped nature of the shear zone mimic the characteristics of a propagating density current (Simpson 1969). Parsons et al. (1991) presented observational evidence that supported the contribution of density current dynamics to the retrograding dryline at the leading edge. The UMass

224

METEOROLOGICAL MONOGRAPHS

Vol. 33, No. 55

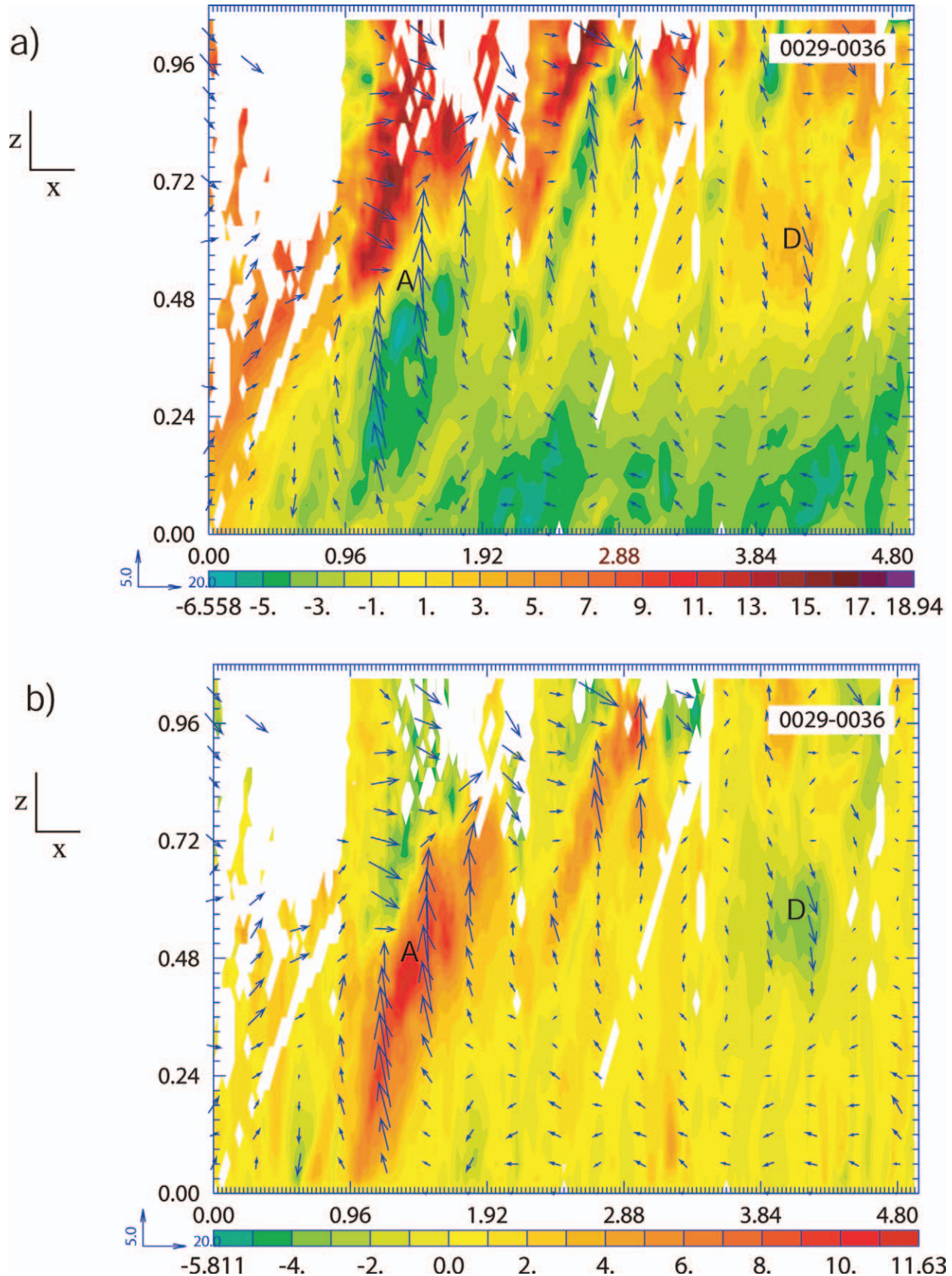


FIG. 19. (a) Ground-relative u -component wind (m s^{-1} ; contoured) and (b) w -component wind (m s^{-1} ; contoured) from the variational analysis of the rolling RHI. Cool colors indicate negative component, warm colors indicate positive component. The arrows in (a) and (b) represent u/w wind vectors. Horizontal and vertical distance scales (km AGL) are indicated. Grid points with fewer than 10 radial velocity observations have been omitted. The areas of strong ascent (A) and descent (D) are identified.

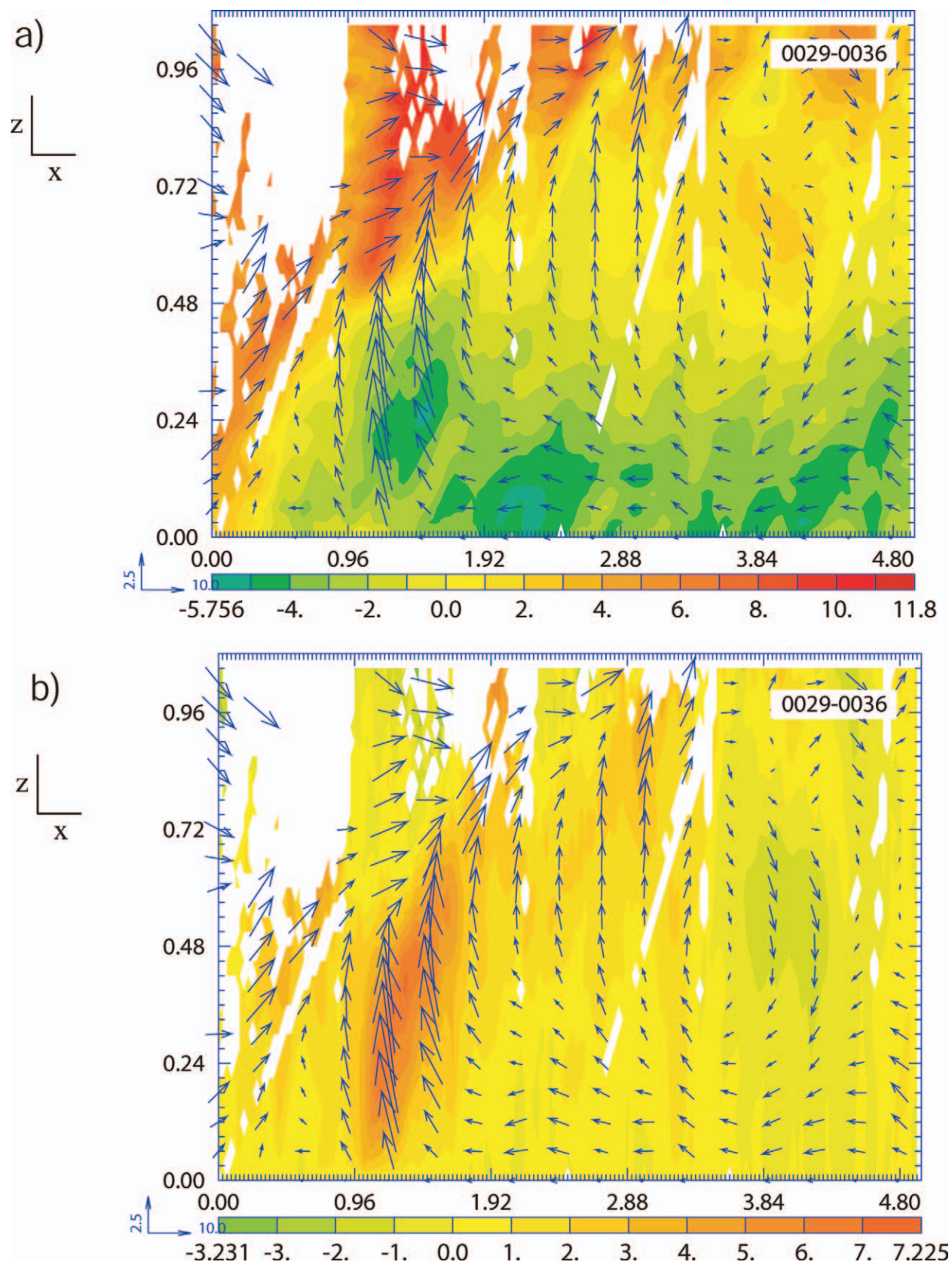


FIG. 20. Same as in Fig. 19, but for analyses with $\beta = m(\Delta x)^2$, where β denotes the relative impact of radial velocity observation (cf. the mass continuity constraint) in the calculation of the cost function, m is the number of radar observations at each analysis point, and Δx is the grid spacing of the analysis.

and UWKA/WCR observations in this study also qualitatively support this hypothesis. However, fine-resolution thermodynamic measurements in the boundary layer are necessary to assess more firmly the validity of density current theory. Attempts to retrieve pressure perturbations from these pseudo-multiple-Doppler analyses were largely unsuccessful because the western extent of the analysis domain was not far enough west of the DCZ to calculate the dryline-normal pressure gradient, nor was it possible to identify accurately a base state ahead of the retreating dryline to use as a boundary condition for the retrieval integration (Parsons et al. 1991).

Acknowledgments. This work was supported by National Science Foundation (NSF) Grants ATM-9912097 and ATM-0241037 (to the University of Oklahoma), and ATM-0129374 (to the University of Wyoming), and was part of the first author's doctoral dissertation at the University of Oklahoma. We are in debt to Evgeni Fedorovich, Carl Hane, Alan Shapiro, David Stensrud, Baxter Vieux, and Conrad Ziegler for useful advice. Dave Leon was instrumental in the WCR intercomparison efforts. Evgeni Fedorovich and Bob Conzemius provided LES data for the testing of the variational analysis scheme. Rick Damiani created the single- and dual-Doppler processing algorithms for the WCR data. Thanks also to David Dowell for his useful insight into variational radar data processing. Curtis Alexander, Nettie Arnott, Mike Buban, Yvette Richardson, and Josh Wurman all assisted in providing mobile radar locations and orientations for the 22 May 2002 case. Paul Markowski provided guidance on GIS applications used in the truck pitch correction. Ming Xue assisted in the use of ZXPLLOT, which was used to create the analysis figures. Brendan Fennell drove the UMass vehicle for the 22 May 2002 data collection. We also appreciate the computer support from Mark Laufersweiler at the School of Meteorology.

REFERENCES

- Atkins, N. T., R. M. Wakimoto, and C. L. Ziegler, 1998: Observations of the finescale structure of a dryline during VORTEX 95. *Mon. Wea. Rev.*, **126**, 525–550.
- Biggerstaff, M. I., and Coauthors, 2005: The Shared Mobile Atmospheric Research and Teaching Radar: A collaboration to enhance research and teaching. *Bull. Amer. Meteor. Soc.*, **86**, 1263–1274.
- Bluestein, H. B., 2008: Surface boundaries of the Southern Plains: Their role in the initiation of convective storms. *Synoptic-Dynamic Meteorology and Weather Analysis and Forecasting: A Tribute to Fred Sanders, Meteor. Monogr.*, No. 55, Amer. Meteor. Soc.
- , and A. L. Pazmany, 2000: Observations of tornadoes and other convective phenomena with a mobile, 3-mm wavelength, Doppler radar: The spring 1999 field experiment. *Bull. Amer. Meteor. Soc.*, **81**, 2939–2952.
- Cohn, S. A., W. O. J. Brown, C. L. Martin, M. E. Susedik, G. Maclean, and D. B. Parsons, 2001: Clear air boundary layer space antenna wind measurement with the Multiple Antenna Profiler (MAPR). *Ann. Geophys.*, **19**, 845–854.
- Crawford, T. M., and H. B. Bluestein, 1997: Characteristics of dryline passage. *Mon. Wea. Rev.*, **125**, 463–477.
- Demoz, B., and Coauthors, 2006: The dryline on 22 May 2002 during IHOP_2002: Convective-scale measurements at the profiling site. *Mon. Wea. Rev.*, **134**, 294–310.
- Dowell, D. C., and H. B. Bluestein, 2002: The 8 June 1995 McLean, Texas, storm. Part I: Observations of cyclic tornadogenesis. *Mon. Wea. Rev.*, **130**, 2626–2648.
- Feltz, W. F., H. B. Howell, R. O. Knuteson, H. M. Woolf, and H. E. Revercomb, 2003: Near continuous profiling of temperature, moisture, and atmospheric stability using the Atmospheric Emitted Radiance Interferometer (AERI). *J. Appl. Meteor.*, **42**, 584–597.
- Gao, J., M. Xue, A. Shapiro, and K. K. Droegemeier, 1999: A variational method for the analysis of three-dimensional wind fields from two Doppler radars. *Mon. Wea. Rev.*, **127**, 2128–2142.
- Geerts, B., and Q. Miao, 2005: The use of millimeter Doppler radar echoes to estimate vertical air velocities in the fair-weather convective boundary layer. *J. Atmos. Oceanic Technol.*, **22**, 225–246.
- Hane, C. E., C. L. Ziegler, and H. B. Bluestein, 1993: Investigation of the dryline and convective storms initiated along the dryline: Field experiments during COPS-91. *Bull. Amer. Meteor. Soc.*, **74**, 2133–2145.
- , H. B. Bluestein, T. M. Crawford, M. E. Baldwin, and R. M. Rabin, 1997: Severe thunderstorm development in relation to along-dryline variability: A case study. *Mon. Wea. Rev.*, **125**, 231–251.
- , M. E. Baldwin, H. B. Bluestein, T. M. Crawford, and R. M. Rabin, 2001: A case study of severe storm development along a dryline within a synoptically active environment. Part I: Dryline motion and an Eta model forecast. *Mon. Wea. Rev.*, **129**, 2183–2204.
- Hildebrand, P. H., and Coauthors, 1996: The ELDORA/ASTRAIA airborne Doppler weather radar: High-resolution observations from TOGA COARE. *Bull. Amer. Meteor. Soc.*, **77**, 213–232.
- Jorgensen, D. P., T. J. Matejka, and J. D. DuGranrut, 1995: Multi-beam techniques for deriving wind fields from airborne Doppler radars. *J. Meteor. Atmos. Phys.*, **58**, 83–104.
- LeMone, M. A., 1973: The structure and dynamics of horizontal roll vortices in the planetary boundary layer. *J. Atmos. Sci.*, **30**, 1077–1091.
- , F. Chen, J. G. Alfieri, M. Tewan, B. Geerts, Q. Miao, R. L. Grossman, and R. L. Coulter, 2007: Influence of land cover and soil moisture on the horizontal distribution of sensible and latent heat fluxes in southeast Kansas during IHOP_2002 and CASES-97. *J. Hydrometeorol.*, **8**, 68–87.
- Miller, D. A., and F. Sanders, 1980: Mesoscale conditions for the severe convection of 3 April 1974 in the east-central United States. *J. Atmos. Sci.*, **37**, 1041–1055.
- Parsons, D. B., M. A. Shapiro, R. M. Hardesty, R. J. Zamora, and J. M. Intrieri, 1991: The finescale structure of a west Texas dryline. *Mon. Wea. Rev.*, **119**, 1283–1292.
- Russell, R. W., and J. W. Wilson, 1997: Radar-observed “fine lines” in the optically clear boundary layer: Reflectivity contributions from aerial plankton and its predators. *Bound.-Layer Meteorol.*, **82**, 235–262.
- Sanders, F. S., 1986: Temperatures of air parcels lifted from the surface: Background, application and nomograms. *Wea. Forecasting*, **1**, 190–205.
- , and A. J. Garrett, 1975: Application of a convective plume model to prediction of thunderstorms. *Mon. Wea. Rev.*, **103**, 874–877.
- , and D. O. Blanchard, 1993: The origin of a severe thunderstorm in Kansas on 10 May 1985. *Mon. Wea. Rev.*, **121**, 133–149.
- , and C. A. Doswell, 1995: A case for detailed surface analysis. *Bull. Amer. Meteor. Soc.*, **76**, 505–522.

- Sasaki, Y., 1970: Some basic formalisms in numerical variational analysis. *Mon. Wea. Rev.*, **98**, 875–883.
- Simpson, J. E., 1969: A comparison between laboratory and atmospheric density currents. *Quart. J. Roy. Meteor. Soc.*, **95**, 758–765.
- Weckwerth, T. M., and Coauthors, 2004: An overview of the International H₂O Project (IHOP_2002) and some preliminary highlights. *Bull. Amer. Meteor. Soc.*, **85**, 253–277.
- Weiss, C. C., and H. B. Bluestein, 2002: Airborne pseudo-dual Doppler analysis of a dryline–outflow boundary intersection. *Mon. Wea. Rev.*, **130**, 1207–1226.
- , —, and A. L. Pazmany, 2006: Finescale radar observations of the 22 May 2002 dryline during the International H₂O Project (IHOP). *Mon. Wea. Rev.*, **134**, 273–293.
- Wilson, J. W., and W. E. Schreiber, 1986: Initiation of convective storms by radar-observed boundary layer convergence lines. *Mon. Wea. Rev.*, **114**, 2516–2536.
- Ziegler, C. L., W. J. Martin, R. A. Pielke, and R. L. Walko, 1995: A modeling study of the dryline. *J. Atmos. Sci.*, **52**, 263–285.